Electronic structure of clean and Ni-O decorated stepped Rh(5 5 3) surfaces

Diplomarbeit

von
Margareta Wagner

zur Erlangung
des akademischen Grades einer Magistra
an der Naturwissenschaftlichen Fakultät der
Karl-Franzens-Universität Graz

Betreuer
O. Univ.-Prof. Dr. phil. Falko P. Netzer
Institut für Physik

2008

Preface

This work investigates nanostructures on surfaces. In surface science the interest is focused on the first few atomic layers of a material, where interactions of the solid with atoms and molecules of the ambient vapor take place (e. g. oxidation). To keep these processes under control and to ensure a clean surface as a reference, surface science methods have to be performed in ultra-high vacuum. There, processes like the growth of thin film of atoms or molecules, or chemical processes like oxidation and reduction of the surface, can be studied in a well-defined way. Several parameters, which influence the kinetics of growth and reactions are tunable, such as the substrate temperature, the flux of evaporation, or the partial pressure of an induced gas. A field of surface science, where research has been intensified within the past years, is the creation of nanostructures: On a scale of length nanostructures are $<$100 nm (at least in one dimension), and can be classified into zero-dimensional (single atoms), one-dimensional (atomic chains, 'nanowires'), two-dimensional (ultra-thin films), and three-dimensional (small cluster) structures. The interest on such structures follows different purposes: In industry, miniaturization is an often stressed keyword in the production of micro chips (Moore's law from 1965 concerning the number of transistors per chip still comes true [1]), in catalytic processes (e. g. car engines), etc. Reasons for the extensive basic research are novel physical and chemical properties of a material when the size of a structure is reduced to a small cluster, a chain of atoms or even a single atom.

This work is focused on the creation of 1D and 2D lateral nanostructures and their electronic structure. One of the simplest 1D systems are stepped surfaces, where the atoms along the step edges are the intrinsic nanowires. Investigations on vicinal surfaces of noble metals, such as stepped Cu(1 1 1) and Au(1 1 1) surfaces have been done by [2, 3, 4, 5]. A prevalent method to create 1D atomic chains on a surface via hetero-epitaxy is the decoration of

monoatomic step edges of a vicinal substrate. The regular step array of the template leads to a spatial separation of the chains of several atomic distances (depending on the terrace width of the stepped surface), which is usually sufficient to prevent interaction of the nanowires with each other. Within the last few years electronic (and magnetic) properties of such heterogeneous 1D systems have been investigated by ARPES, for example Fe/Au(7 8 8) [6, 7], Co/Pt(9 9 7), and Au/Si(5 5 7) [2].

In this work, the materials of the stepped surface and the step decoration are a Rh(5 5 3) single crystal and Ni of high-purity, which is deposited via physical vapor deposition. The experiments have been performed under ultra-high vacuum conditions.
The late transition metals Ni and Rh are important materials used in catalysis, basic research on e. g. the oxidation of Rh(5 5 3) with high oxygen pressure (with respect to the pressure of UHV) has been reported by Gustafson et al. [8], or the chemical reactivity of Ni wires on vicinal Rh(1 1 1) surfaces, which has been investigated by Schoiswohl et al. [9].

The aim of this diploma thesis was to investigate the electronic structure of one-dimensional Ni-wires attached to the step edges of a well ordered vicinal Rh(5 5 3) substrate: The electronic structure of the clean an Ni-decorated surfaces has been measured by angle-resolved UPS and compared to DFT calculations. Earlier studies on the system Ni/Rh(5 5 3) have been performed by J. Schoiswohl, a former member of the research group at the Karl-Franzens-University Graz. Almost the whole literature on the system Ni/Rh(5 5 3) includes his investigations, which have been performed mainly by scanning tunneling microscopy and X-ray photoelectron spectroscopy. Survey spectra of the valence band have been measured with a synchrotron radiation source (at a different photon energy as used in the laboratory for this work), but without angular resolution.

Basic literature on the system Ni/Rh(5 5 3): [9, 10, 11]

Contents

Part I

Introduction

Chapter 1

Theory of Experimental Techniques

1.1 Introduction

Nowadays there are several experimental techniques which are commonly used to determine the properties of a surface (a thin film etc.) such as morphology, order/disorder, orientation and symmetry, electronic states, etc.
For this work spectroscopic methods (which are related to the reciprocal space) have been used to determine the electronic structure of one-dimensional Ni chains attached to step edges of a vicinal Rh(5 5 3) substrate (single crystal).

1.2 Direct and Reciprocal Space

A crystal is defined as an (quasi) infinite three-dimensional periodic arrangement of small units such as atoms, molecules etc. In a more precise description the crystal consists of a three dimensional point lattice and a basis (single or group of atoms, molecules etc.) sitting on each lattice point. The three shortest distances (vectors) between the origin of the lattice (arbitrary lattice point) to the nearest lattice points in three dimensions define the lattice vectors $\vec{a}_i$ with magnitudes a_i (i. e. lattice constants), where $i = 1$, 2, or 3 labels the direction in space.
For Bravais lattices it is possible to identify each lattice point with a linear combination of these vectors $\vec{a}_i$.

$$\vec{R} = m\vec{a}_1 + n\vec{a}_2 + o\vec{a}_3 \qquad m, n, o \in \mathbb{Z} \tag{1.1}$$

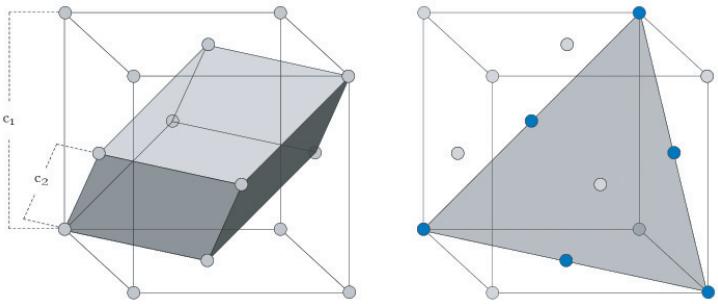

Figure 1.1: Left: Primitive (parallelepiped) and conventional (cubic) unit cell of the fcc lattice. Right: Conventional unit cell with (1 1 1) plane (blue lattice points).

The vectors $\vec{a}_i$ also form the so-called *primitive unit cell* which is the smallest repeating unit within the lattice and it contains only one lattice point. Often a *conventional unit cell* which is non-primitive is assumed for a better understanding of the symmetry.
For a face centered cubic (fcc) lattice, as Rh crystallizes in, the conventional unit cell is four times the volume of the primitive one. Fig. 1.1 shows both cells of this symmetry. The lattice constants are the length of the cube and the distance between two adjacent lattice points.

For a discussion of diffraction on periodic structures (see textbooks like [12]) and for the interpretation of diffraction patterns an introduction of the appropriate reciprocal lattice is fundamental. The reciprocal lattice can be understood as the Fourier transformation of the Bravais lattice. The primitive unit cell in reciprocal space with a lattice point in its origin is the *first Brillouin zone*. For the fcc crystal the bulk Brillouin zone is illustrated in Fig. 1.2 as well as the surface Brillouin zone of the (1 1 1) plane.

The nomenclature for the vectors in reciprocal space corresponding to the set of $\vec{a}_i$ in real space, is $\vec{b}_i$. They are defined by the following properties:

$$\vec{a}_i \cdot \vec{b}_k = 0 \qquad \text{for } i \neq k \tag{1.2}$$

$$\vec{a}_i \cdot \vec{b}_i = 2\pi \tag{1.3}$$

where $i, k \in \{1, 2, 3\}$.
The vanishing scalar product in equation (1.2) defines each vector $\vec{a}_i$ perpendicular to two vectors $\vec{b}_i$ in reciprocal space. Equation (1.3) sets the norm for $\vec{b}_i$. According to this $\vec{b}_i$ must be considered to have the value

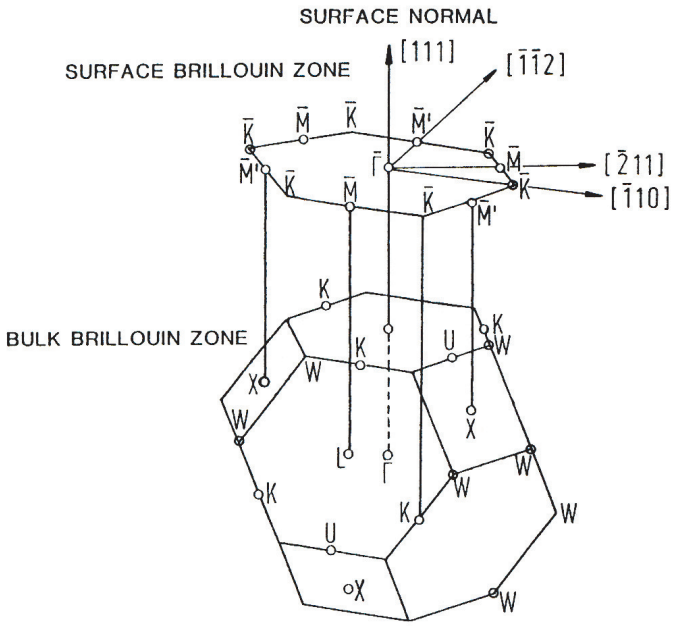

Figure 1.2: First Brillouin zone of the fcc bulk and surface zone of the (1 1 1) plane. Figure taken from [13].

$2\pi/(a_i \sin(\angle \vec{b}_i, \vec{a}_i))$ for the projection on the direction i, where a_i is the magnitude of $\vec{a}_i$.

If $\vec{R}$ are vectors of the Bravais lattice in real space, reciprocal space consists of all vectors $\vec{G}$ when the following equation is fulfilled (which is a result of Fourier transformation of a Bravais lattice and translational symmetry).

$$e^{i \cdot \vec{G} \cdot \vec{R}} = 1. \tag{1.4}$$

$$\vec{G} \cdot \vec{R} = 2\pi c \qquad c \in \mathbb{Z}. \tag{1.5}$$

and with the volume of the unit cell $V_c = \vec{a}_1(\vec{a}_2 \times \vec{a}_3)$ the following vectors $\vec{b}_i$ satisfy this condition:

$$\begin{aligned} \vec{b}_1 &= \frac{2\pi}{V_c}(\vec{a}_2 \times \vec{a}_3) \\ \vec{b}_2 &= \frac{2\pi}{V_c}(\vec{a}_3 \times \vec{a}_1) \\ \vec{b}_3 &= \frac{2\pi}{V_c}(\vec{a}_1 \times \vec{a}_2) \end{aligned} \tag{1.6}$$

A reciprocal lattice vector can be specified as

$$\vec{G} = h\vec{b}_1 + k\vec{b}_2 + l\vec{b}_3. \tag{1.7}$$

Expanding equation (1.5) leads to

$$\vec{G} \cdot \vec{R} = 2\pi(hm + kn + lo) = 2\pi c \qquad c \in \mathbb{Z} \tag{1.8}$$

which implies h, k, and l have to be integer. They are the so-called *Miller indices* of a lattice plane and are written as a triple (h k l).
An important[1] plane within a crystal with fcc symmetry is the close-packed (1 1 1) plane with hexagonal symmetry, which is indicated in the right panel of Fig. 1.1.

When surfaces are described, usually the direction perpendicular to the surface is neglected although relaxation processes often result in a change of the atomic distance of the topmost layers in z-direction. However, the symmetry of the surface and therefore its unit cell is given by two vectors $\vec{a}_1$ and $\vec{a}_2$ and corresponding reciprocal vectors $\vec{b}_1$ and $\vec{b}_2$. The vectors $\vec{b}_i$ are a consequence of equation (1.6):

$$\vec{b}_1 = 2\pi\left(\frac{\vec{a}_2 \times \vec{n}}{\vec{a}_1(\vec{a}_2 \times \vec{n})}\right), \text{ and } \vec{b}_2 = 2\pi\left(\frac{\vec{n} \times \vec{a}_1}{\vec{a}_2(\vec{n} \times \vec{a}_1)}\right) \tag{1.9}$$

where $\vec{n}$ is a unit vector normal to the surface.

Hence, the lattice of a surface with the third dimension equal to zero consists of lattice rods instead of lattice points in k-space. Diffraction on surfaces will be discussed later on (Chapter 1.4) where we will see that this 'property' results in a diffraction pattern for every energy of the incident beam.

The lattice of a hexagonal surface like the fcc (1 1 1), is described in direct space and k-space as drawn in Fig. 1.3. With $\hat{x}$ and $\hat{y}$ being unit vectors in x and y-direction, the angle $2\alpha = 60\,^\circ$, the vectors $\vec{a}_1$ and $\vec{a}_2$ are given by

$$\vec{a}_1 = -a_1(\sin\alpha\hat{x} + \cos\alpha\hat{y}), \text{ and } \vec{a}_2 = a_2\hat{x} \tag{1.10}$$

and in reciprocal space

$$\vec{b}_1 = -\frac{2\pi}{a_1\cos\alpha}\hat{y}, \text{ and } \vec{b}_2 = \frac{2\pi}{a_2}\left(\hat{x} - \tan\alpha\hat{y}\right). \tag{1.11}$$

[1] Important for this work, since the terraces of the used crystal are (111) planes.

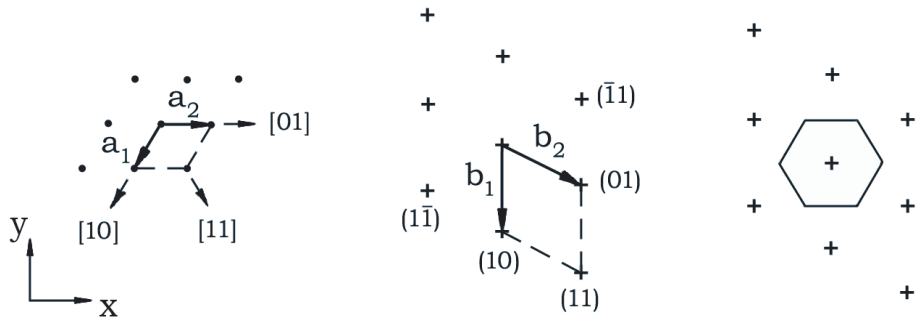

Figure 1.3: Hexagonal lattice in direct and reciprocal space. The vectors of the primitive unit cells (left: real space, middle: reciprocal space) and the first Brillouin zone (right) are indicated (figure taken from [12]).

1.3 Stepped Surfaces

When a plane is cut by a small angle θ with respect to a low-index plane like the $\{1\,1\,1\}$ or $\{1\,0\,0\}$ the surface consists of N atoms wide terraces with the symmetry of the low-index plane, separated by steps of height h (e. g. monoatomic steps). The lattice periodicity (lattice constant a) is superimposed by the larger repeating unit of the step array. For small miscut angles the density of steps is low and the ledges are well separated; in this case the enthalpy of the surface increases proportional to the density of steps. Forming steps on a surface also increases the entropy. In combination enthalpy and entropy result in a surface energy proportional to θ. In other words, when a step is created (or any other new piece of surface) the atoms sitting right along the edge have more broken bonds (due to less neighbors) than the atoms within the surface. For a crystal with fcc symmetry (coordination number 12), the atoms within the $(1\,1\,1)$ surface have three broken bonds (coordination number 9) and the atoms of step edges with $(1\,1\,1)$ facets five (coordination number 7).
Another effect is that step atoms or adatoms are able to vibrate more freely than terrace atoms.
Summarizing, the surface energy of a flat surface (h k l) is always smaller than the surface energy of a surface vicinal to the (h k l)-plane. In the following, the surface energy is regarded as an excess *free* energy per unit area which is the energy per unit area one has to afford when breaking the bonds in creating a surface (and the interface is in thermodynamic equilibrium).

The density of steps is defined as the number of steps per unit length

$$\text{Step density} := \frac{\tan\theta}{a} \tag{1.12}$$

with a as the length of the unit cell and θ the inclination angle, compare Fig. 1.4 (a). The surface tension of the vicinal surface consists of three main terms: The surface tension of the flat surface γ_0 (with terrace symmetry), the tension of the step γ_1, and a term describing the interaction of the steps with each other, plus terms of high-order.

$$\gamma = \cos\theta\left[\gamma_0 + \gamma_1\frac{\tan\theta}{a} + \gamma_2\left(\frac{\tan\theta}{a}\right)^2 + \cdots\right] \tag{1.13}$$

In the case of wide terraces and/or weak interaction between the steps, the terms describing the interaction can be neglected and (1.13) simplifies to

$$\gamma(\theta) = \gamma_0\cos\theta + \frac{\gamma_1}{a}\sin\theta. \tag{1.14}$$

The surface tension of the steps can be written as $\gamma_1 = \eta E_1$ where η is a phenomenological parameter that quantifies the entropy of the step (including effects of temperature[2]), and E_1 is the excess energy per unit length of the edge. The term for the surface energy changes to

$$\gamma(\theta) = \gamma_0\cos\theta + \frac{\eta E_1}{a}\sin\theta \tag{1.15}$$

and is referred to as the *Gruber-Mullins theory* (e. g. [14]). The ability for a step edge to roughen, i. e. forming kinks, depends on the interaction between the steps and thus on the spacing between them. Increasing θ and therefore decreasing the terrace width, the edges become straight to avoid interaction (i. e. overlapping).

The surface energy (tension) as a function of θ (i. e. the lattice plane of the surface) is depicted in the so called the Wulff plot. For a simple cubic solid which is slightly miscut to a (14) surface (terraces have [01] orientation) the two-dimensional Wulff plot according to equation (1.15) is shown in Fig. 1.4 (b). The surface energy obviously maximizes for $\theta = 45\,^\circ$ where the step density maximizes (steps are of monoatomic height and the terraces one atom wide). The plot has the same rotational symmetry as the surface. The absolute value of the radius vector from the origin to a point on the plot

[2] At $T = 0\,\mathrm{K}$ there is no contribution of entropy, steps and kinks do not wander and $\eta = 1$. For finite temperatures $\eta < 1$.

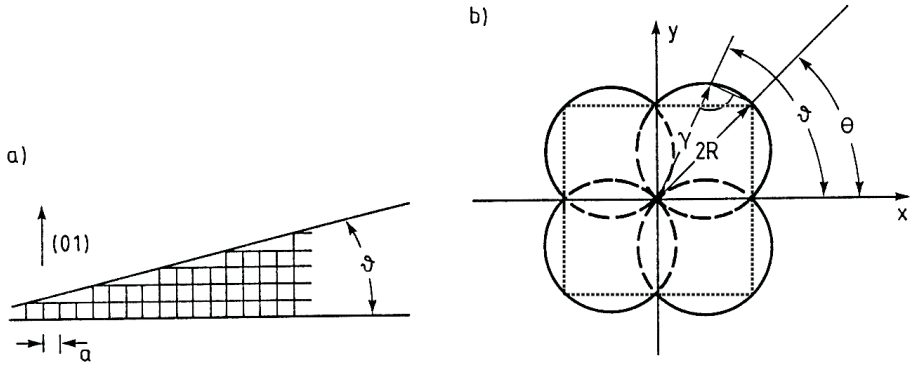

Figure 1.4: (a) Schematic drawing of a vicinal surface. (b) Wulff plot relating to the vicinal surface. For $\theta = 45\,^\circ$ the surface energy is maximal. Figure taken from [16].

represents the magnitude $\gamma(\theta)$ which is $\gamma(\mathrm{h\,k\,l})$ (in the direction normal to the (h k l)-plane).

For θ equal zero (low-index plane) equation (1.15) has a discontinuous derivative

$$\Delta \left(\frac{\mathrm{d}\gamma}{\mathrm{d}\theta} \right)_{\theta=0} = \frac{2\gamma_1}{a} \tag{1.16}$$

which means a cusp in the plot. Its magnitude $\gamma_{\theta=0}$ is proportional to the increase of the free energy for each additional edge [15].

For $T \neq 0$ in equilibrium a crystal of fixed volume strives to form the shape that minimizes

$$\oint \gamma(\theta)\mathrm{A}. \tag{1.17}$$

The equilibrium shape consists of planes with minimum surface tension. It can be drawn easily on the basis of the Wulff plot by following the procedure of the Wulff construction, which has been described elsewhere [15, 17, 16]. In short, one draws planes perpendicular to all vectors in the Wulff plot. The inner envelope determines the surfaces which fulfill equation (1.17). The surface however does not necessarily form only planes with low surface tension; in some cases it might be thermodynamically favored to form facets in order to minimize the total surface energy. For the example of the vicinal (14) surface the equilibrium shape is a square.

To form the equilibrium shape according to the Wulff construction it is sufficient for atoms to diffuse fast enough all over the surface to reach the site of lowest energy. This primarily applies for small crystallites and clusters at high temperature, whereas the shape of crystals is highly determined by the kinetics of epitaxy, i. e. the growth rate of different lattice planes (slowly growing planes which often have low surface energy as well survive) and not the Wulff construction.

1.4 Low Energy Electron Diffraction

In surface science it is a matter of particular interest to get information on the symmetry of the topmost layer of a crystal, and to detect changes due to well ordered adsorbats or tiny amounts of an additional material on the surface. For these investigations diffraction is the method of choice. Depending on the scattered particle (electron, neutron) one can analyze different aspects of the symmetry and geometry of the surface or bulk of a sample.

For the present investigations a surface sensitive diffraction method is necessary and Low Energy Electron Diffraction (LEED) is the common used tool.
The degree of surface sensitivity is measured by the mean free path λ of electrons, which is related to the penetration depth in z-direction (perpendicular to the surface). Inelastic processes (i. e. plasmons) happening in the surface region cause a decrease of the elastically scattered intensity. The origins of these inelastic processes do not necessarily have to be known perfectly well when the matter is treated in a more theoretical way, but all together they are described by an imaginary part of the electron-surface interacting potential. These processes obviously depend on the energy of the electrons and therefore the mean free path shows this behavior as well. On the other hand, the penetration depth varies very little with the element for most metallic surfaces and this is why a 'universal curve', illustrated in Fig. 1.5, for the mean free path dependence of the electron energy can be drawn (with a common imaginary part of the interacting potential of 1–5 eV) [12].
The energy regime of LEED is 10–200 eV where the mean free path is 5–20 Å. This allows the determination of the symmetry of the first few top layers of a sample.

A sketch of the experimental equipment of a common LEED apparatus is given in Fig. 1.6. The surface is bombarded with monochromatic electrons

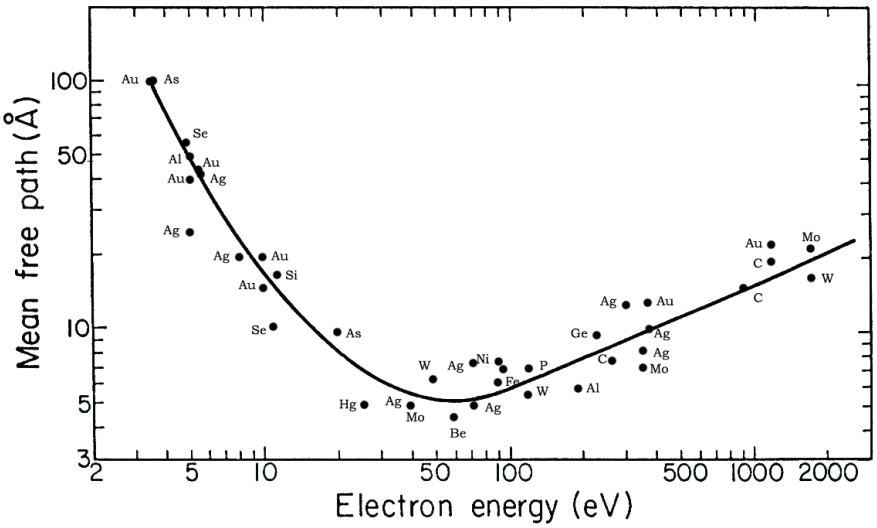

Figure 1.5: 'Universal curve': Dependence of λ on electron energy. LEED operates in the range of 10–200 eV.

coming from a heated filament and monochromatized by applying a voltage (0–300 V). The electron beam is focused on the sample. The scattered electrons have to pass potential grids where inelastically scattered electrons are caught. Only electrons which are scattered elastically reach the Micro Channelplate (MCP) and the fluorescent screen behind it (for the LEED used here). Due to the fact that MCP and screen are flat in contrast to the hemispheric grids, the diffraction pattern appears distorted. A fringe correction leads to nearly parallel trajectories of the electrons between the last grid and MCP, and a linear correlation of the radial distance (from the center of the optics to a spot) on the screen and the last grid is provided.

$$k_{\parallel}^{screen} = c k_{\parallel}^{grid} \qquad c \text{ is const.} \tag{1.18}$$

Since the electron beam usually has a spot size of 1–2 mm^2 on the sample, LEED averages over this large area (compared to distances within the microscopic surface) and shows the most prevalent symmetries.

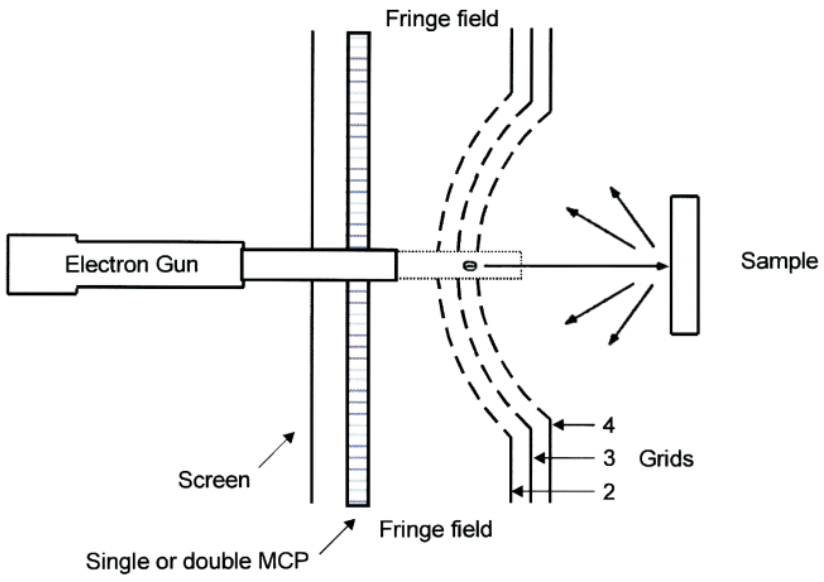

Figure 1.6: Schematic construction of a LEED (figure taken from manual).

1.4.1 Common Superstructures on Hexagonal Surfaces

When the symmetry of the surface is described by vectors $\vec{a}_i$ in real space, and $\vec{b}_i$ in reciprocal space, the symmetry of the superlattice is described with respect to the substrate symmetry. If the $\vec{s}_i$ describe the additional layer, they are written as

$$\vec{s}_i = m_{i1}\vec{a}_1 + m_{i2}\vec{a}_2 \tag{1.19}$$

where the m_{ij} can be combined into a matrix

$$M = \begin{pmatrix} m_{11} & m_{12} \\ m_{21} & m_{22} \end{pmatrix}. \tag{1.20}$$

When a clean surface is exposed to an ambient gas, adsorbed atoms or molecules may form well ordered superstructures, depending on parameters such as temperature, gas pressure and time of exposure. The same applies for deposited material via evaporation. In many cases the additional layers are visible in the LEED by means of extra spots corresponding to the symmetry within the layer with.

In the following, two superstructures which often appear on surfaces with hexagonal symmetry will be discussed in direct and reciprocal space, respectively. In most cases both structures result in the same LEED pattern,

although they belong to a different adsorbate coverage. If the absolute coverage of the adatoms is not known, the two structures cannot be distinguished by observing the LEED pattern only.

The (2×2) Structure

A very common and simple superstructure with the coverage of a quarter of a monolayer has a (2×2) symmetry. The upper panel of Fig. 1.7 illustrates this structure in direct and reciprocal space for the case of adatoms sitting in on-top sites. The vectors of the unit cell of the superstructure are twice as long as the substrate vectors and the repeating cell has four times the size of the substrate unit cell. In matrix notation, the structure obviously has the items

$$M = \begin{pmatrix} 2 & 0 \\ 0 & 2 \end{pmatrix}. \tag{1.21}$$

The (2×1) Structure

The (2×1) superstructure corresponds to a coverage of one half of a monolayer. The unit cell is a parallelogram, where one side is the substrate lattice constant and the other one is twice as long. Its size is two times the substrate unit cell. Due to the hexagonal symmetry there are three different arrangements or domains possible which are rotated by $60\,^\circ$ with respect to each other.
In matrix notation, the three domains are characterized by

$$\begin{aligned} \mathbf{M}_\triangle = \begin{pmatrix} 2 & 0 \\ 0 & 1 \end{pmatrix},\ \mathbf{M}_\bigcirc = \begin{pmatrix} 1 & 0 \\ 2 & 2 \end{pmatrix}, \\ \mathbf{M}_\square = \begin{pmatrix} 1 & 1 \\ 0 & 2 \end{pmatrix} \end{aligned} \quad . \tag{1.22}$$

Fig. 1.8 illustrates the LEED pattern for each domain where the lattice vectors of the substrate (dotted) and superlattice (solid line) are indicated. In the cartoon of real space adatoms are assumed to occupy top sites. The whole diffraction pattern is shown in the bottom part of Fig. 1.7. The symbols $\triangle$, $\bigcirc$, and $\square$ are extra spots corresponding to the domain structure. Solid dots are both diffraction spots of the substrate and the superstructure .

In the case of well ordered domains of a size smaller than the instrumental transfer width, different domains contribute coherently to the diffraction. As

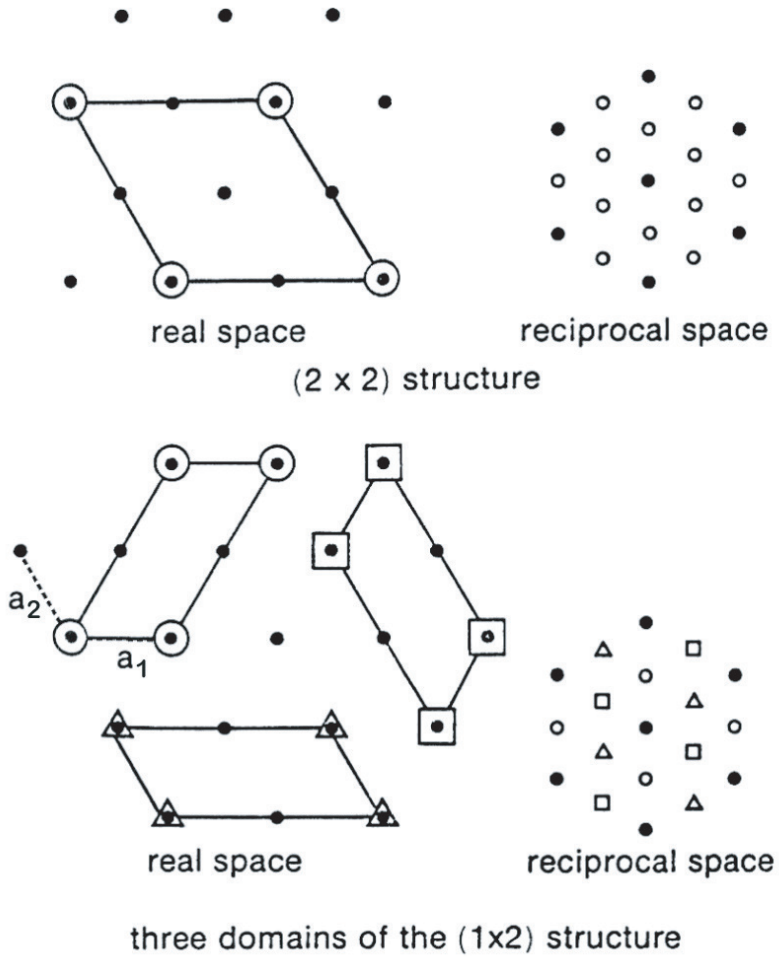

Figure 1.7: (2×2) and (2×1) superstructure on a fcc $(1\,1\,1)$ surface. In direct space, the unit cells of the overlayer are indicated, and the vectors which describe the substrate, $\vec{a}_1$ and $\vec{a}_2$ (dotted). In reciprocal space, the solid dots are diffraction spots of the substrate, while the symbols correspond to additional spots (figure taken from [12]).

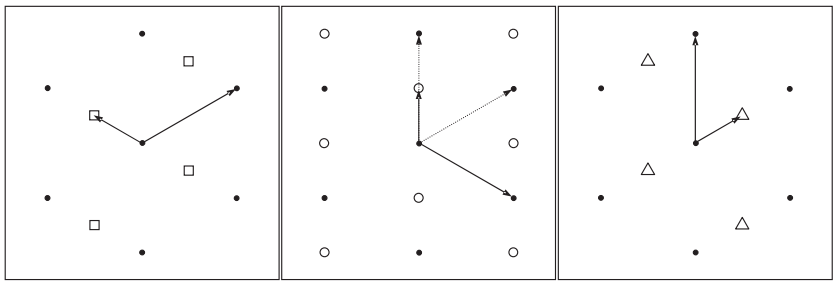

Figure 1.8: The three domains of the (2×1) structure: The vectors corresponding to the substrate (panel in the middle; dashed) and those of the domains (solid) are indicated. The symbols refer to Fig. 1.7.

a consequence, the periodicity of the domain size causes narrow split spots. For this treatment here, the size of domains can be presumed to be larger than the transfer width of the instrument (which is about 200 Å). This causes diffraction within different domains to happen independently and the total pattern is an addition of intensities (instead of diffracted amplitudes with relative phases and interference) of the single patterns.
Only in this second case the diffraction pattern is equal to the pattern of the (2×2) structure.

1.4.2 Ewald Construction

The diffraction pattern of vicinal surfaces as well as origin, position and spacing of the spots can be understood intuitively with the concept of the Ewald sphere. Therefore elastic scattering of the incidence electrons is assumed and—as a first approximation—the interacting area of the crystal with the electrons is simplified to be 2 dimensional (no dimension in z-direction, i. e. perpendicular to the surface).
The Ewald construction for a surface with low Miller indices (i. e. flat surface) and a vicinal surface will be discussed in the following.

For a flat surface the Ewald construction along a high symmetry direction is shown in Fig. 1.9. In reciprocal space the lattice points of the surface (single layer of atoms) become rods perpendicular to the surface.
The momentum $\vec{k}_0$ of the incident electrons with absolute value $|\vec{k}_0|$ is indicated in the figure, pointing at the (00) lattice rod. Since LEED deals with elastic scattering, the diffracted electrons also have the absolute value

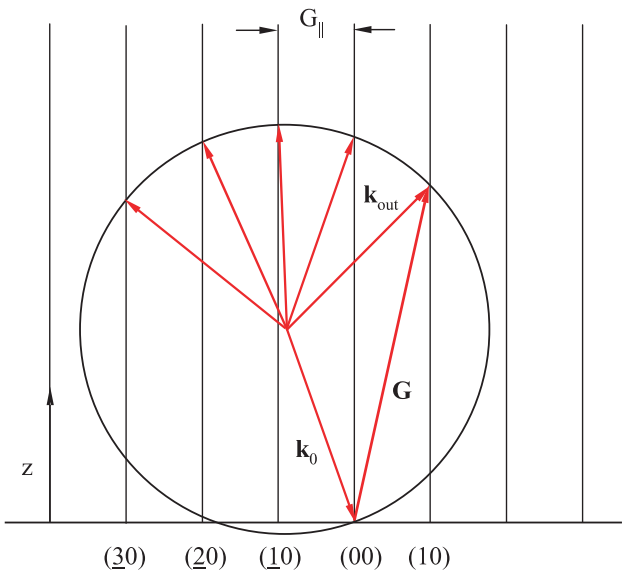

Figure 1.9: Ewald construction of a flat surface. Diffraction spots appear on the intersection points of the sphere with lattice rods.

$|\vec{k}_0| = |\vec{k}_{out}|$ and the momentum vector may point everywhere within the sphere of radius $|\vec{k}_0|$. To get a diffraction spot the condition for constructive interference (von Laue) must be accomplished. Constructive interference happens for

$$(\vec{k}_{out} - \vec{k}_0)\vec{R} = \vec{K}\vec{R} = 2n\pi \qquad n = 1, 2, \ldots \tag{1.23}$$

which is equivalent to equation 1.4

$$e^{i(\vec{k}_{out} - \vec{k}_0)\vec{R}} = 1 \tag{1.24}$$

and that is complied for

$$\vec{k}_{out} - \vec{k}_0 = \vec{K} = \vec{G}. \tag{1.25}$$

Neglecting the third dimension a spot is achieved for vectors k_{out} pointing at an intersection point of the Ewald sphere with a lattice rod, wherefore $K_{\|} = G_{\|}$ is fulfilled.

When the energy of the electrons increases and the pattern is projected on a LEED screen the spots move toward the (00) spot which is immobile.

For the treatment of the stepped surface with a miscut angle α with respect to a high symmetry plane, let us assume that the surface faces the

LEED screen with the vicinal surface (i. e. the saw tooth which is the macroscopic and optical surface) and not the terraces.
Vicinal surfaces are interpreted not as a single array of lattice rods, but as a surface with the terrace symmetry combined with a 'superstructure' corresponding to the step array [12, 18, 19]. Thus, in reciprocal space the surface consists of two arrays of lattice rods which are inclined with respect to each other by an angle α, as illustrated in Fig. 1.10. The solid rods correspond to the terrace atoms and have the spacing of the reciprocal lattice vector $G_{\|}$. The dotted species belongs to the periodicity of the steps and the spacing of the rods is $Q = 2\pi/Na$ for terraces of width Na.

Bragg spots only appear when constructive interference happens for both terrace atom rods and rods of the macroscopic surface. For infinite sharp lattice rods (i. e. infinite number of diffraction centers) this only happens at intersection points of the Ewald sphere with both types of rods which would cause just a few single spots. However, the intensity distribution (width) of the rods depends on the number of diffraction centers; an infinite terrace would have rods described by delta functions, but as the terraces of vicinal surfaces have small width the terrace rods are broad and blurred in intensity. The theoretical treatment of the matter deals with the convolution of the lattices in real space, and after Fourier transformation into k-space one has to multiply the of arrays of not infinitely sharp rods (e. g. [20]).

Going back to the Ewald picture a reflection can be expected at the rods of the macroscopic surface. They are strong in intensity when they are close to the terrace atoms' rods (i. e. a value of the convolution not equal to zero), and weak or invisible in-between them. Depending on the energy of the electrons one usually observes up to three spots at one location (fixed at the macroscopic surface rod). With changing energy the intensity and number of components changes (and there is an additional modulation due to the z-periodicity).
There are two situations which can be distinguished:

- A terrace and a macroscopic surface rod intersect the Ewald sphere at the same point; in this case one bright spot is observed, and, depending on the width of the terraces maybe two weak spots on both sides (green in Fig. 1.10).

- A terrace rod intersects the sphere in-between the intersection points of the next neighboring macroscopic surface rods. Due to the blurred lattice rods this results in two spots of equal intensity, as shown in the red example of Fig. 1.10.

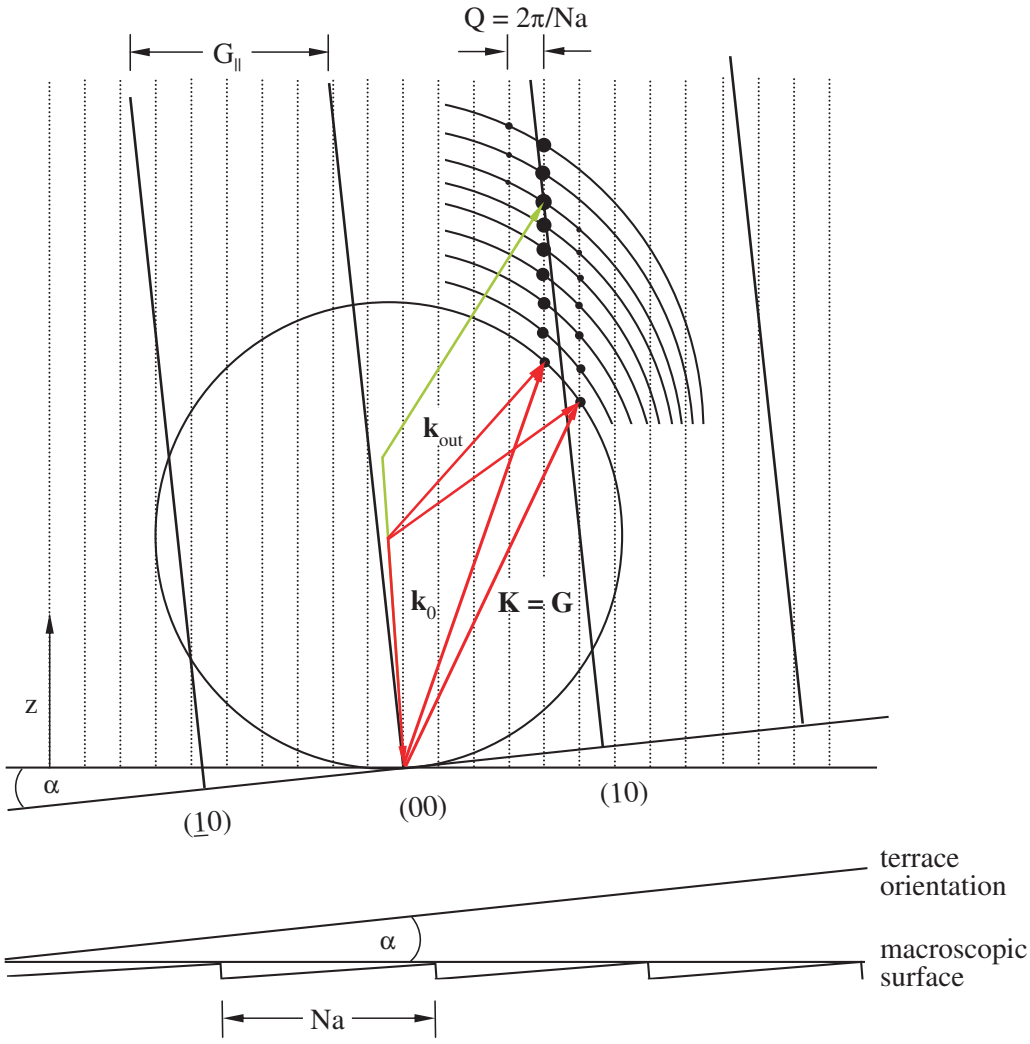

Figure 1.10: Top: Ewald construction of a vicinal surface. Intense spots are indicated (•) for several electron energies along the Ewald circle. Bottom: Alignment of the surface corresponding to the Ewald construction.

In the second case, the angle $\delta\varphi$ between the split spots can be measured and the width of the terraces determined.

$$\delta\varphi = \frac{Q}{k_{out}\cos\varphi} = \frac{Q}{k_i\cos\varphi} = \frac{\lambda}{Na\cos\varphi} \tag{1.26}$$

with λ as the wavelength of the electrons, φ the average scattering angle of the split spot, and Na the terrace width.

There is an energy dependence of spot locations and spot components. With increasing kinetic energy of the electrons the whole diffraction pattern follows two evolutions: The locations of groups of spots (which are around terrace rods) move toward the (00)-spot of the terrace, while the spots themselves (macroscopic surface rods) converge toward the specular of the macroscopic surface, corresponding to Fig. 1.11 [12].
This behavior (and in consequence the orientation of the crystal, whether is faces the LEED with the terraces or the macroscopic surface) can be determined easily by comparing LEED patterns at different electron energies (see Chapter 2.2, Fig. 2.6).

1.4.3 Interpretation of LEED Pattern

Although the Ewald construction leads to a good understanding not only of the diffraction pattern but also the geometry of vicinal surfaces, the unit cell of a stepped surface will be analyzed now in more detail following the procedure of reference [12].
Therefore two vectors in real space are assumed, forming the unit cell of the step array: $\vec{e}$ is parallel to the step edges, while $\vec{w}$ lies in the macroscopic surface plane (and not the terrace plane) connecting two equivalent atoms of adjacent edges, and its magnitude gives the width of the terrace. The vector $\vec{w}$ is not necessarily perpendicular to $\vec{e}$.
The stepped surface has Miller indices (h k l), the terraces are ($\mathrm{h}_t\,\mathrm{k}_t\,\mathrm{l}_t$) oriented. With the appropriate vectors $\vec{u} = (\mathrm{h\,k\,l})$ and $\vec{u}_t = (\mathrm{h}_t\,\mathrm{k}_t\,\mathrm{l}_t)$, $\vec{e}$ can be calculated as following:

$$\vec{e} = \pm\frac{q_t}{p}\vec{u}_t \times \vec{u} \tag{1.27}$$

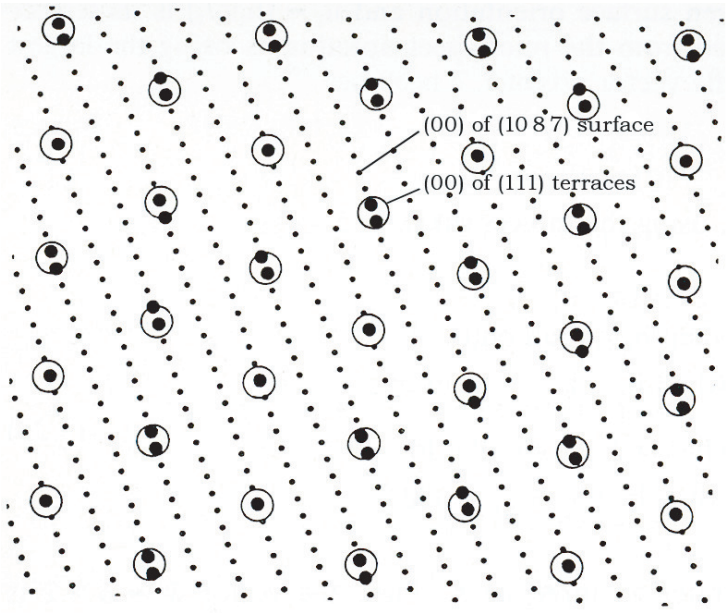

Figure 1.11: Diffraction pattern of a vicinal fcc (10 8 7) surface. Circles indicate locations of terrace rods ('top view') with bright diffraction spots at macroscopic surface rods (•); macroscopic surface rods without visible spot are drawn smaller (figure taken from [12]).

where q_t and p are defined by the Miller indices $(\mathrm{h_t\,k_t\,l_t})$ and $(\mathrm{h\,k\,l})$, respectively.

$$p = \begin{cases} 1 \text{ for } \begin{cases} \text{sc lattices,} \\ \text{bcc lattices, when h+k+l is odd.} \end{cases} \\ 2 \text{ for } \begin{cases} \text{fcc lattices, when h, k, l are not all odd,} \\ \text{bcc lattices, when h+k+l is even.} \end{cases} \\ 4 \text{ for } \quad \text{fcc lattices when h, k, l are all odd.} \end{cases} \tag{1.28}$$

$$q_t = \begin{cases} 1 \text{ for } \begin{cases} \text{sc,} \\ \text{fcc, when } \mathrm{h_t,\ k_t,\ l_t} \text{ are all odd,} \\ \text{bcc, when } \mathrm{h_t{+}k_t{+}l_t} \text{ is even.} \end{cases} \\ 2 \text{ for } \begin{cases} \text{fcc, when } \mathrm{h_t,\ k_t,\ l_t} \text{ are not all odd,} \\ \text{bcc, when } \mathrm{h_t{+}k_t{+}l_t} \text{ is odd.} \end{cases} \end{cases} \tag{1.29}$$

To build vector $\vec{w}^*$, at first $\vec{w}' = \vec{u} \times \vec{e}$ is formed and scaled to $\omega\vec{w}'$ to satisfy the relation for ω: $|\omega\vec{w}' \times \vec{e}| = |\vec{u}|\,/p$; and ω becomes the inverse of an integer $n = 1/\omega$. Now $\vec{w}$ is obtained to be $\vec{w} = \omega(\vec{w}' + m\vec{e})$, and the integer $m \in (1,\, n)$ is varied until $\vec{w}$ becomes a lattice vector of the crystal structure.

In reciprocal space, the unit cell of the step array is formed by the following vectors, using equation (1.9):

$$\vec{e}^* = 2\pi\frac{\vec{w} \times \vec{u}}{\vec{e}(\vec{w} \times \vec{u})} \qquad \textit{and} \qquad \vec{w}^* = 2\pi\frac{\vec{u} \times \vec{e}}{\vec{e}(\vec{w} \times \vec{u})} \tag{1.30}$$

The vector $\vec{e}^*$ describes the largest distance in reciprocal space, which corresponds to the atomic distance within the terraces.
The vector $\vec{w}^*$ is perpendicular to the real step edge and identifies the splitting of the spots in the diffraction pattern. The magnitude w^* which is the distance between the components of the split spots is correlated to the width of the terraces, w, by $w = 2\pi/w^*$. By definition, w is measured parallel to the macroscopic surface and perpendicular to the step edge.
The diffraction pattern of a vicinal (10 8 7) surface is illustrated in Fig. 1.11: The distance of atoms within the (1 1 1) terrace corresponds to the distance between two circles, while the terrace width is given by the spot splitting.

The inclination angle between the macroscopic surface $(\mathrm{h\,k\,l})$ and its terraces $(\mathrm{h_t\,k_t\,l_t})$ is

$$\cos\alpha = \frac{\vec{u}\vec{u}_t}{|\vec{u}|\,|\vec{u}_t|}, \tag{1.31}$$

and the height of the steps can be determined by

$$d = \frac{1}{q_t \, |\vec{u}_t|}. \tag{1.32}$$

1.5 Photoelectron Spectroscopy

Photoelectron spectroscopy (PS) is a powerful tool to characterize the electronic structure of a surface. For this method the sample is irradiated with light of a certain energy and the excited electrons are detected (outer photoelectric effect). Depending on the energy of the irradiation one can probe chemical or electronic properties.

The chemical aspects are investigated by core level spectroscopy, which means electrons of the core levels are excited. This is done with X-ray irradiation and the common name is X-ray Photoelectron Spectroscopy (XPS). Core levels are discrete and the energy of the orbitals is sensitive to the chemical element and to changes, like for example oxidation or alloy formation. Not only the energy of the state but also the shape of the spectrum is characteristic for a certain chemical state. X-ray sources in the laboratory are the characteristic spectral lines of metals such as Al K_α (1486.6 eV) or Mg K_α (1253.6 eV).
To investigate the electronic structure of a system, the valence band of the material is of particular interest. Electrons of the valence band have a low binding energy and ultraviolet light (in the range lower than 100 eV) is able to excite only these valence electrons and no deep core level electrons. Therefore valence band spectroscopy is called Ultraviolet Photoelectron spectroscopy (UPS). Common sources of highly ($\sim$meV) monochromatic radiation in the laboratory are noble gas discharge lamps.
In photoemission, a large fraction of the signal originates from the first few layers of the crystal, i. e. the surface. When a photoelectron is excited, it might lose a certain amount of kinetic energy by inelastic scattering processes on its way to the surface. The deeper the photoelectron comes from the crystal, the higher is the probability of losing a large amount of its energy. At some point the electron has lost too much energy to overcome the work function and is not able to escape the crystal any more.

1.5.1 Excitation Process

The commonly used model to describe the photoemission process of an electron from a solid is the three-step model (developed by Berglund and Spicer). Although the photoemission is a one-step process the model has been proven to be quite successful with its splitting-up of the photoemission process into excitation of an electron, passing through the solid, and escape into vacuum. The dominant optical excitations in the UPS regime are direct, which means momentum of the final state $\vec{k}_f$ is equal to the initial momentum $\vec{k}_i$. In the reduced zone scheme these transitions are 'vertical', for the extended zone scheme vectors of the reciprocal lattice have to be added and $\vec{k}_f = \vec{k}_i + \vec{G}$. In the following $\vec{G}$ is a vector of the reciprocal lattice, $\vec{k}$ is the crystal momentum, $\vec{K}$ the momentum of the photoexcited electron within the crystal, and $\vec{p}$ the final momentum of the electron outside the crystal.

The first step describes the absorption of a photon by an electron in the solid. Due to energy conservation during the excitation and momentum conservation (momentum of the photon can be neglected since it is small with respect to the electron's momentum) which causes the $\delta(E_f - E_i - h\nu)\,\delta(E - (E_f - \phi))$ and $\delta(\vec{k}_i + \vec{G} - \vec{K})$ terms in equation (1.33) and (1.41) (with the energies E_i and E_f of initial and final bands, respectively). The second delta function in the energy term sets the kinetic energy outside the sample equal to the final state energy. Inside the crystal the energy distribution of photoexcited electrons (in reduced zone scheme) can be expressed by

$$\begin{aligned} N_{int}(E, h\nu) &= \sum_{f,i} \left| M^1_{fi}(\vec{k}_i, \vec{k}_f) \right|^2 \\ &\quad \times \delta(E_f(\vec{k}_f) - E_i(\vec{k}_i) - h\nu)\,\delta(E - [E_f(\vec{k}_f) - \phi]) \end{aligned} \quad (1.33)$$

where $|M^1_{fi}(\vec{k}_i, \vec{k}_f)|$ is the transition matrix element of the interacting operator (nonlinear processes are neglected).

In the second step, the transport of the excited electron to the surface is described. The dominant effects which reduce the number of excited electrons are electron-electron interaction and, close to the threshold, phonons. These electrons form the secondary electron background of the spectrum, whose intensity increases with decreasing kinetic energy. Electrons which are photoexcited within the mean free path are able to reach the surface without any further interaction, and they carry information about the initial state. Assuming the mean free path $\lambda(E, k)$ with the scattering frequency

$1/\tau$, with τ as the lifetime,

$$\lambda(E,k) = (\tau/\hbar)\,\mathrm{d}E/\mathrm{d}k = \tau v_g^f \tag{1.34}$$

with v_g^f as the group velocity of the final state. In the classical treatment of Berglund and Spicer the transport is described as the fraction of the total number of photoelectrons created within one mean free path λ. With the optical absorption coefficient α the coefficient $\mathrm{d}(E,k)$ describes the transport by

$$\mathrm{d}(E,k) \simeq \frac{\alpha\lambda}{1+\alpha\lambda}. \tag{1.35}$$

In the third step of the model the escape of the electron from the crystal is treated. Electrons which have a component of the kinetic energy perpendicular to the surface which is at least the surface potential $\hbar^2\vec{K}_\perp^2/(2m) \geq E_{vac} - E_0$ (the energy of the bottom of the valence band $E_0 < 0$) are able to leave the crystal. Electrons with less energy are reflected. When the electron is transmitted through the surface, momentum parallel to the surface is conserved. This can be graphically shown with the escape-cone-argument (see [13]), whereby $\vec{p}_\parallel/\hbar = \vec{K}_\parallel = \vec{k}_\parallel + \vec{G}_\parallel$. Assuming the free electron model for the excitation, for the magnitude of the parallel component of momentum, Fig. 1.12 and Snell's law give

$$k_\parallel = \sin\vartheta \left(\frac{2m}{\hbar^2}E_{kin}\right)^{1/2} = \sin\vartheta' \left(\frac{2m}{\hbar^2}(E_f - E_0)\right)^{1/2}. \tag{1.36}$$

This well-known equation connects the angular dependence of detected photoelectrons with their momentum, and this is fundamental for angle-resolved PS experiments. Fig. 1.12 shows the momentum relations at the interface, where ϑ' is the angle inside and ϑ outside the solid. Since the angle ϑ is larger with respect to the surface normal than ϑ', there is (for a given energy of the final state) a maximum angle $\vartheta'_{max} < \pi/2$ at which photoelectrons can escape through the surface into vacuum. The maximum escape angle ϑ is 90 ° which corresponds to the maximum parallel component of momentum.

$$\sin\vartheta'_{max} = \left(\frac{E_{kin}}{E_f - E_0}\right)^{1/2} \tag{1.37}$$

The kinetic energy of an electron of a final state of energy E_f outside the crystal is

$$E_{kin} = E_f(\vec{k}) - E_{vac} = \frac{\hbar^2}{2m}\left(\vec{K}_\parallel^2 + (\vec{p}_\perp/\hbar)^2\right) \tag{1.38}$$

where $\vec{p}_\perp/\hbar$ is the perpendicular component of the electron's momentum outside the crystal. The momentum of the electron perpendicular to the

surface inside the crystal cannot be determined since the momentum $\vec{k}_\perp$ of the crystal state is not known.
Taking into account that the wave function of a state $E_f(\vec{k})$ in a 'real' solid is not a single plane wave but a Bloch wave with reciprocal vectors $\vec{G}$

$$\psi_f(\vec{k}) = \sum_{\vec{G}} u_f(\vec{k}, \vec{G}) e^{i(\vec{k}+\vec{G})\vec{r}} \tag{1.39}$$

which causes different possible directions for an electron referring to the components of the wave; components with the same value $\vec{k}_\parallel + \vec{G}_\parallel$ and the energy E run in the same direction and are coherent. Summing the transmission factors for each plane wave (with a component propagating perpendicular to the surface) gives the total transmission factor for a beam with $\vec{k}_\parallel + \vec{G}_\parallel$ and can be expressed as

$$\left|T(E_f, \vec{k}_\parallel)\right|^2 = \left|t(E_f, \vec{K}_\parallel)\right|^2 \left| \sum_{(\vec{k}+\vec{G})_\perp > 0} u_f(\vec{G}, \vec{k}) \right|^2 . \tag{1.40}$$

The model results in a final expression for the intensity $I(E, \vec{K}_\parallel, h\nu)$ of angle-resolved photoemission, with $h\nu$ as the photon energy:

$$\begin{aligned} I(E, \vec{K}_\parallel, h\nu) \;\propto\; & \sum_{f,i} \left|M^1_{fi}(\vec{k}_i, \vec{k}_f)\right|^2 \mathrm{d}(E_f, \vec{k}_f) \left|T(E_f, \vec{K}_\parallel)\right|^2 \\ & \times \delta(E_f(\vec{k}_f) - E_i(\vec{k}_i) - h\nu)\, \delta(E - [E_f(\vec{k}_f) - \phi]) \\ & \times \delta(\vec{k}_i + \vec{G} - \vec{K})\, \delta(\vec{K}_\parallel - \vec{p}_\parallel(\vartheta, \varphi)/\hbar) \end{aligned} \tag{1.41}$$

where $\delta(\vec{K}_\parallel - \vec{p}_\parallel(\vartheta, \varphi)/\hbar)$ expresses the conservation of momentum for the component parallel to the surface. The matrix element contains only the general conservation rule of $\vec{k}$, while the third step of the model explicitly deals with the conservation of the parallel component $\vec{k}_\parallel$. Inside the crystal $\vec{K}_\parallel = \vec{k}_{i\parallel} + \vec{G}_\parallel$, and outside $\vec{p}_\parallel(\vartheta, \varphi)/\hbar = \vec{K}_\parallel$. The angles ϑ and φ indicate the direction of the detected electrons.

1.5.2 Work Function

With both XPS and UPS the work function of a surface can be measured. The work function is the amount of energy in electron volts it costs to remove an electron of an uncharged solid from the Fermi edge to the vacuum level of the surface, $\phi = E_{vac} - E_F$. Speaking of surfaces and surface sensitive

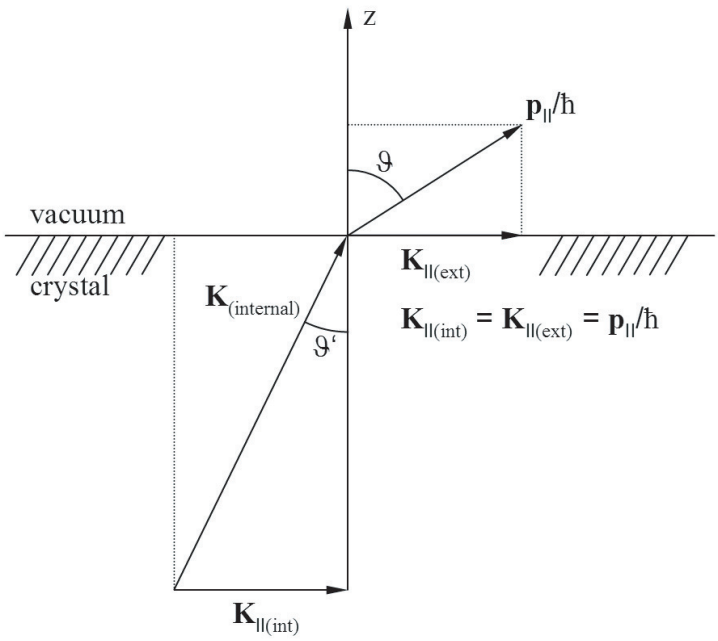

Figure 1.12: Conservation of $k_{\parallel}$.

methods in this work, it is obvious that the work function depends on the surface itself, whether it is open (low work function) or close-packed (atoms are strongly bound which causes high work function), and the contribution of the surface dipole due to the spill-out of conduction electrons.

UPS spectra (intensity versus kinetic energy) of metals show a very characteristic shape: The electrons of highest kinetic energy (photon energy) are emitted from the Fermi edge where the binding energy is zero. The Fermi edge represents one boundary of the spectra. To escape the solid, the energy of an electron must be at least the work function (plus the binding energy for electrons below the Fermi edge). This condition determines the other boundary of the spectra in the low kinetic energy range. In addition to the deep valence band electrons, secondary electrons are created due to inelastically scattered electrons on their way to the surface leading to a very sharp cut-off. The width of the spectra is given by the energy of the incident photons minus the work function), but due to effects in the electron energy analyzer, the secondary electron cut-off might be distorted for materials with a low work function; in this case the work function has to be measured after applying a bias in order to shift the spectrum toward higher kinetic energy.

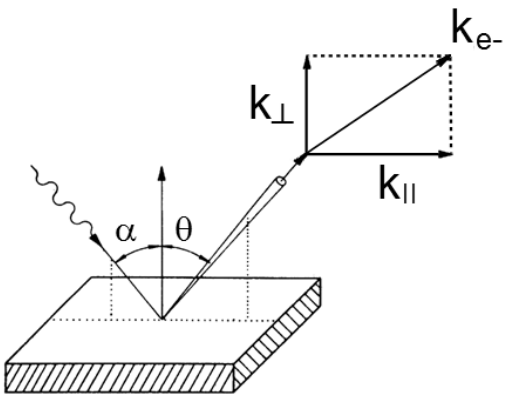

Figure 1.13: Setup for angle-resolved UPS.

The work function is calculated from the width of the spectrum d and the energy of the UV-light $E = h\nu$ by

$$\phi = E - d = E - (E_F - E_{cut}). \tag{1.42}$$

1.5.3 ARUPS and Band Structure

Electronic band structures can be measured with angle-resolved UPS. A detector collects the excited electrons not only as a function of their kinetic energy distribution but also as a function of the emission angle. Changing the detection angle results in probing momentum.

In the experiment the incoming (unpolarized) light and the surface normal enclose a certain angle α which is commonly chosen to be $60\,^\circ$ to achieve equal components of linear polarized light. The detector is rotated in the plane around the sample (also see Fig. 1.13) to probe k-space in the direction parallel to the surface.
The kinetic energy of an electron is given with

$$E = h^2/2m \times (k_\parallel^2 + k_\perp^2). \tag{1.43}$$

When an electron escapes the solid only momentum parallel to the surface is conserved due to the lack of translation symmetry perpendicular to the surface.
The relationship between momentum parallel to the surface $k_\parallel$, kinetic energy, and emission angle θ allows to plot the band structure as an intensity map with binding energy versus momentum.

Basically there are two ways to measure the band structure (or valence band spectra generally) with AREPS, depending on the experimental setup and possibilities. In the common laboratory the analyzer, which is an electron multiplier with small acceptance angle, has to be rotated by hand/motor. At some synchrotron beam lines it is possible to detect the whole emitted electrons (in a certain plane) for all angles at once.
One also can distinguish between normal incidence and off-normal incidence of the irradiation and of course the polarization of the light with respect to the surface.
The probably easiest setup for a common laboratory experiment deals with an angle of incidence α of the UV-light with respect to the surface normal. The emitted electrons can be detected with angular resolution in the range of $\approx \alpha < \theta <$ critical angle (i. e. 70–80 °), including the normal emission.

Measuring band structures with a low photon energy has advantages and disadvantages. One of the most significant advantages is the improved momentum resolution that is a consequence of the laws of momentum conservations. As the photon energy (and therefore the final kinetic energy of the emitted electrons) is decreased, the photoelectrons become more widely dispersed in emission angle. For a given angular resolution of the electron spectrometer the momentum resolution increases with decreasing photon energy. The momentum resolution of ARPES at 21.21 eV (the common He I radiation of a discharging lamp, with angular analyzer acceptance of ± 1 °) is roughly better by a factor of 2 than at 110 eV (which is the 'Cooper minimum' of Rh). For the given instrument it takes 80 spectra to measure the first Brillouin zone (for binding energies close to the Fermi edge), with 110 eV it would take only 34 spectra to cover this region in k-space (with the same angular resultion). A good resolution in momentum also means that less k-space is accessible.
On the other hand, the width of the spectra is given by the photon energy. The lower the photon energy the smaller the range of energy below the Fermi edge one can determine but the valence band extends only a few electron Volts below the Fermi edge.

For the valence band of the system Ni/Rh, examined with He I radiation, the disadvantages mentioned before are of no importance. The major point is that the He I radiation is far away from the Cooper minimum of Rh states, which implies a large signal from the Rh states. Adding a small amount of Ni to decorate the step edges therefore results in small variations of the spectra. With use of synchrotron radiation the excitation energy of the Cooper minimum can be chosen (which means that the photoionization cross section

of certain electron states undergo a minimum) is used to measure partial densities of states of a certain component of a system, for example the Ni adatoms on Rh. This has been done earlier by J. Schoiswohl for the vicinal Rh surface, the decorated surface and after oxidation [10, 9] but not angle-resolved.

1.6 Auger Electron Spectroscopy

Auger electron spectroscopy (AES) is a method to study the chemical composition of the first few atomic layers of a surface.

The surface is bombarded with electrons and the actual Auger process involves three electrons of a surface atom. The first electron (in the core level regime) is removed from the surface and leaves a hole which is filled by an electron from an other (at least the same, or a energetic higher) shell. The energy difference is not emitted as a photon; it is transmitted radiationless to a third electron. This electron, if it has enough energy to leave the surface, is the so called Auger electron; its kinetic energy is given by the energies of the core levels and does not depend on the energy of the irradiated electrons. The nomenclature of Auger electrons refers to the shells that are involved in the process. KLM, for example, means that an electron of a K-level is emitted (first electron), an electron of a L-level occupies the hole (second electron) and the Auger electron itself (third electron) comes from the M-shell.
Since the binding energies of electrons in atoms are specific for each chemical element, peaks of the Auger spectra can be associated with certain elements.

Chapter 2

Experimental Setup

2.1 UHV system: ADES 400 Spectrometer

All experiments have been carried out in UHV with an ADES 400 Spectrometer from VG Scientific. The chamber is evacuated with a rotary pump and an oil diffusion pump, which is continuously cooled with liquid nitrogen. In the chamber one usually has a base pressure in the low 10^{-10} mbar range a few days after a bake-out.
Beside the angle-resolved ultraviolet photoemission spectrometer (ARUPS) this UHV system is equipped with a single Micro Channelplate (MCP) LEED optics (from Omicron), an electron gun for Auger spectroscopy, Ni evaporator (triple evaporator EFM 3T from Omicron), and a quartz microbalance to measure the rate of depositing material, and of course mass spectrometer, sputter gun, manipulator with in-situ rotatable head (and therefore a wobble stick), heating (direct or indirect), and thermocouple connections. A cartoon of the whole system is shown in Fig. 2.1.

Fig. 2.2 shows a photograph of the UHV system. At the bottom and top of the manipulator the x, y, and z drive can be seen and the rotary feedthrough for the rotation of the sample around the vertical axis. In the upper region of the chamber, the sample preparation is done like sputtering and evaporation and rotation of the head of the sample holder. The LEED is mounted on the opposite side of the big window. For AES and UPS measurements the sample is driven down to the bottom region of the chamber, where electron gun, discharge lamp, and the rotatable analyzer are situated. A close-up of at the head of the manipulator (designed for indirect heating via a filament) in the UHV system can be seen in Fig. 2.3. The crystal has two holes and wires through them are spot welded onto a sample plate. The

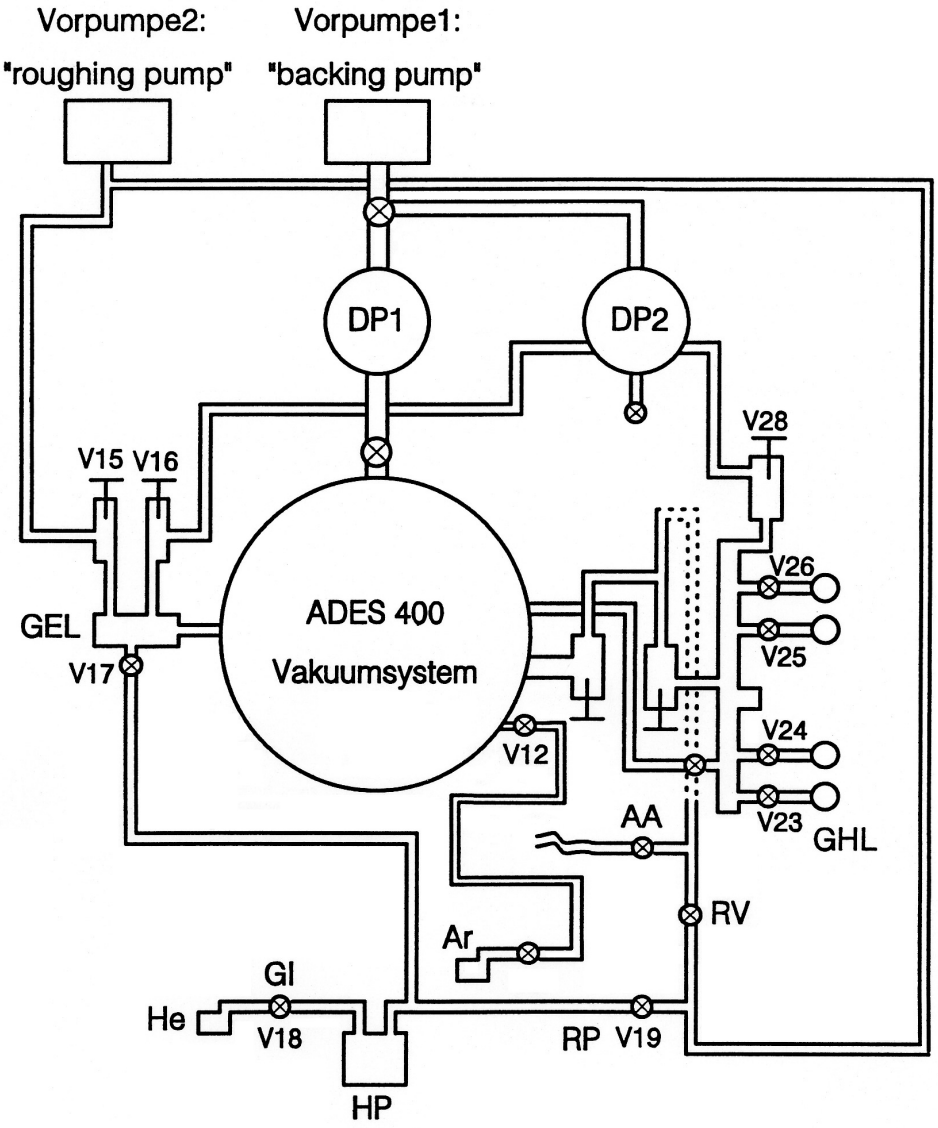

Figure 2.1: Plan of the ADES 400 Spectrometer: DP . . . diffusion pump, V . . . valve, GEL . . . Gasentladungslampe (gas discharge lamp), GHL . . . gas handling line, AA . . . air admit, RV . . . roughing valve, RP . . . roughing purifier, GI . . . lamp gas inlet, HP . . . helium purifier.

whole gray manipulator head is rotable.

The light source of the UPS to generate photoelectrons is a Helium discharge lamp. The He comes from a hight-purity gas bottle and is directed through a cooling trap (cooled with liquid nitrogen) for purification. The light is unpolarized and its energy is 21.21 eV (alpha line of He I). This emission results from the transition of the following configuration of a He atom:

$$1s^1\ 2s^1 \rightarrow 1s^2 + h\nu \tag{2.1}$$

For band structure measurements the analyzer usually is rotated in steps of 1 ° and the acceptance is ±1 °.

2.2 The Rhodium(5 5 3) Surface

Stepped surfaces are obtained when a surface with low Miller indices is cut by a small angle. For the Rh(5 5 3) surface the miscut angle with respect to the (1 1 1) plane is ±12.27 °. Depending on the sign of the miscut angle the steps expose (1 1 1) or (1 0 0) facets. The crystal used in this work has been cut in such a way that the steps form (1 1 1) facets. The surface consists of narrow terraces (5 atoms wide) which are separated by monatomic steps. The terraces are (1 1 1) planes with hexagonal symmetry and an in plane lattice constant of 2.69 Å. The unit cell corresponding to the array of steps is a parallelogram, 2.69 Å wide and 10.42 Å long. A cartoon of the surface is shown in Fig. 2.4 where the unit cell of the terrace atoms and the step periodicity are indicated. STM images in the literature show that this surface forms a very regular step array with almost no kinks and an average terrace width of 10–11 Å [8].

Fig. 2.5 shows the LEED pattern of Rh(5 5 3): The unit cell of the hexagonal symmetry of the terrace atoms (solid line) and of the step array (dashed line) are indicated.
The width of the spot splitting compared to the atomic distance in reciprocal space determines the average width of the terraces (which is approximately the length of the unit cell of the step array). In real space the ratio of the length of the unit cell of the steps and the distance of nearest neighbors on the terraces is calculated to be 3.87. The comparable ratio in reciprocal space (extracted from the LEED pattern) gives the value of 3.8 ± 0.3.

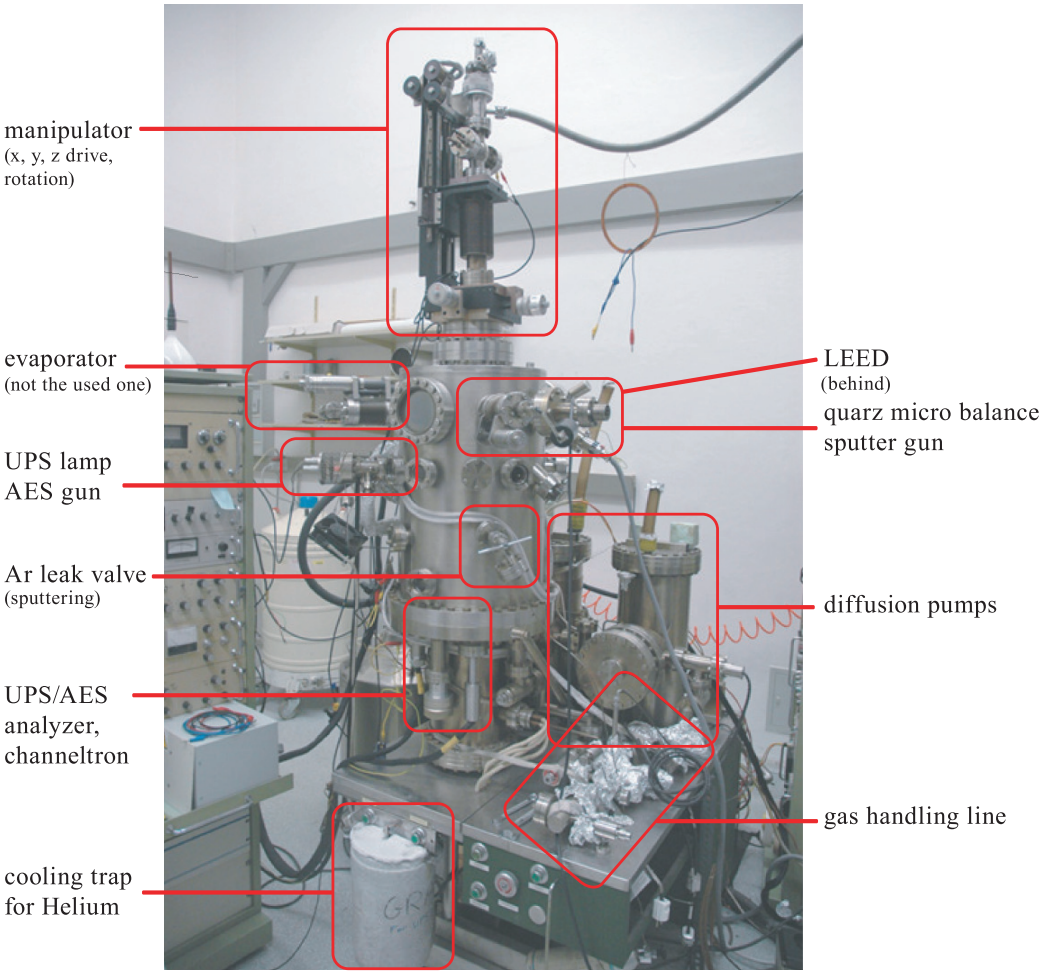

Figure 2.2: Side view of the whole system.

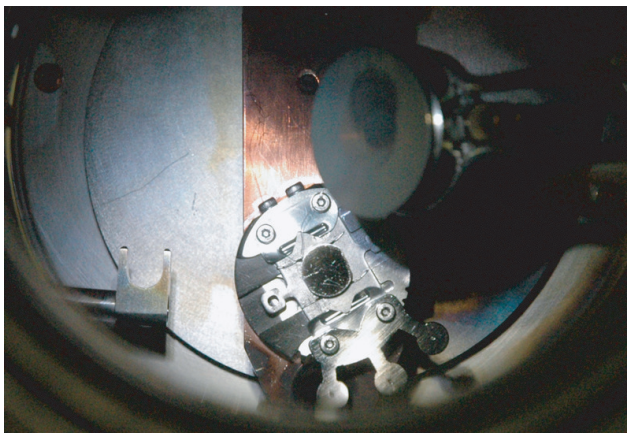

Figure 2.3: Head of the manipulator (with handle bars for the wobble stick to rotate the gray plate which is mounted onto the copper block) with sample plate and mounted crystal, wobble stick on the left side and micro balance on the right side. In the background the shutter which protects the LEED optics can be seen.

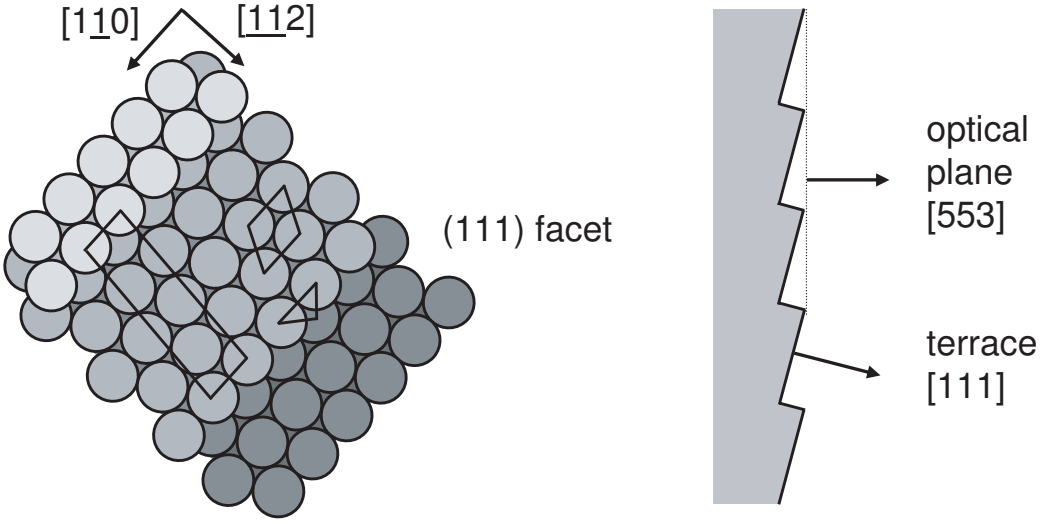

Figure 2.4: Left: Model of the Rh(5 5 3) surface: The unit cell of the terrace atoms (small rhomb) and the step periodicity (parallelogram) are indicated. Right: Schematic side view of the crystal and orientation of the (1 1 1) terraces.

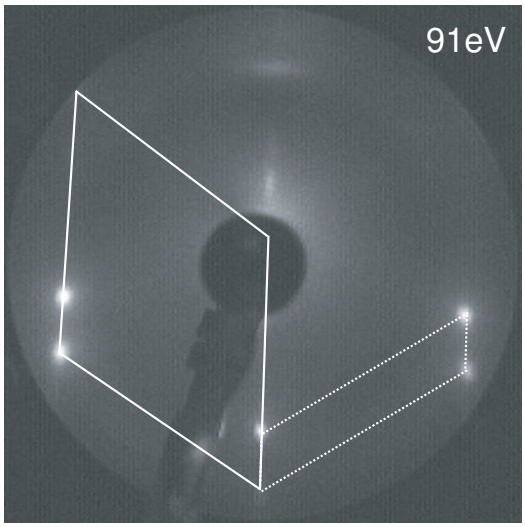

Figure 2.5: LEED image of Rh(5 5 3). The hexagonal unit cell (solid) corresponds to the symmetry on the terraces, while the rhomboid describes the step array (dashed).

The reference direction for the experimental setup for all measurements is the optical surface, which is the (5 5 3) plane (Fig. 2.4, right). According to the Ewald construction for vicinal surfaces (Chapter 1.4.2 and Fig. 1.10) the (0 0) rod of the macroscopic surface (5 5 3) is tilted by $\approx 12^\circ$ with respect to the surface rod of the terraces. This can be seen easily in the LEED pattern by changing the kinetic energy of the electrons. Both spots always stay at the same position on the screen: While the location of the (0 0) lattice rod of the terraces is always visible (beside the de- and increase of intensity of the components due to the splitting), the (0 0) rod of the macroscopic (5 5 3) surface only appears when a terrace rod moves close. However, its position can be defined by plotting diffraction patterns of different electron energies together.
Both evolutions can be seen in Fig. 2.6 where the crystal is rotated to off-normal incidence of the electron beam. The (for most energies) invisible (0 0) spot of the macroscopic surface (where the single spots converge to) is next to the electron gun (left in Fig. 2.6), while the specular beam of the terraces is found below the electron gun (right) (this indicates the orientation of the crystal as shown in Fig. 2.4, right panel). The distance (as an angle) of the electron gun to the terraces' specular spot can be approximated by rotating the crystal: The diameter of the gun has been found to be $\approx 5^\circ$ and therefore the (0 0) spot is $10 \pm 2^\circ$ below the gun.

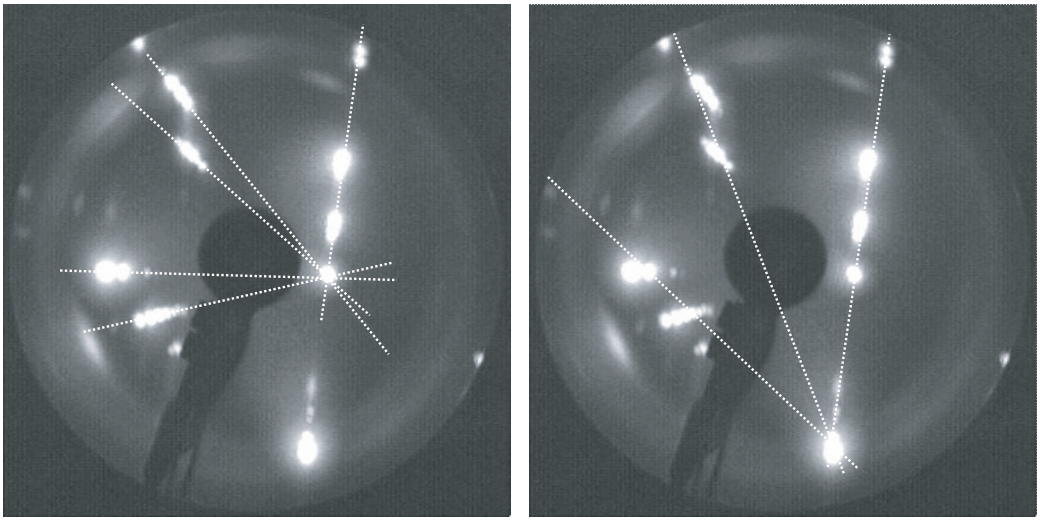

Figure 2.6: LEED pattern of 70–160 eV measured in steps of 10 eV. Single spots move towards the position of the macroscopic surface's specular beam (left), while the spots converge toward the specular reflex of the terraces (right).

2.3 Nickel on Stepped Rhodium Surfaces

A procedure to decorate the Rh steps with Ni has been studied by J. Schoiswohl in Graz and examined by XPS (see [11]). Spectra of the Rh $3d_{5/2}$ core level can be fitted with contributions of bulk atoms, terrace atoms, atoms underneath the step, and step atoms. After decorating the steps with Ni there is no emission from the step sites and their contribution is completely quenched. Two new components appear; they are associated with emission of Rh atoms coordinated to Ni atoms.
Currently[1] there are no STM images available of the Ni decorated Rh(5 5 3) surface, but there are STM images of the Rh(15 15 13) surface, which is similar but has tree times larger terraces. Ni can be seen attached to the step edges and the geometric parameters indicate pseudomorphic growth for small amounts of Ni on Rh [10].

[1] May 2008

2.4 Sample Preparation

2.4.1 Cleaning Procedure

The stepped Rh sample (a precleaned surface, not a freshly polished one) introduced into the UHV system has been cleaned as follows:

1. The crystal was sputtered with Ar^+ ions (500 V), 25 mA emission current for 30–40 min and subsequently flashed to 920 K in UHV both to recover the stepped morphology and bring up carbon to the surface.

2. When the sample was still hot the crystal is exposed to 6 L oxygen (2 min in 5×10^{-8} mbar oxygen pressure) in order to remove carbon atoms via oxidation.

3. To start a new cycle the crystal was flashed to 1020 K in UHV in order to remove the adsorbed oxygen, CO, etc.

After repeating steps 1–3 four or five times the cleaning time was reduced to 10–15 min, and repeated four or five times again. After that the crystal was free of most of the contaminations of the bulk.

Before starting the actual measurements the Rh(5 5 3) crystal was finally flashed to 1020 K in order to remove possibly adsorbants. It was sputtered with 500 V Ar^+ ions for 8 min and subsequently flashed to 920 K.

In literature reports Rh surfaces (even stepped ones) are usually annealed several minutes at 1000–1270 K due to the high melting temperature of Rh of 2237 K. For the given crystal and the present UHV system this procedure has been found to be particularly unfavorable. After annealing at this high temperature complex and large superstructures as well as facets were formed on the crystal (see Fig. 2.7), very likely due to carbon that came up to the surface during heating. Sputtering at room temperature and elevated temperature combined with oxygen treatments (also at various temperatures up to 1270 K) did not solve the problem within two months. According to LEED, AES, and UPS (work function and spectra) the alternative 'low and quick' temperature cleaning procedure described above has been found to lead to a reproducible clean stepped surface.

During the ARUPS measurements the crystal was flashed to 770 K periodically (i. e. every two hours) in order to remove CO that adsorbs from the ambient gas of the UHV. After two hours the work function typically increases by $\approx$0.1 eV although the UPS spectra yet do not show any significant

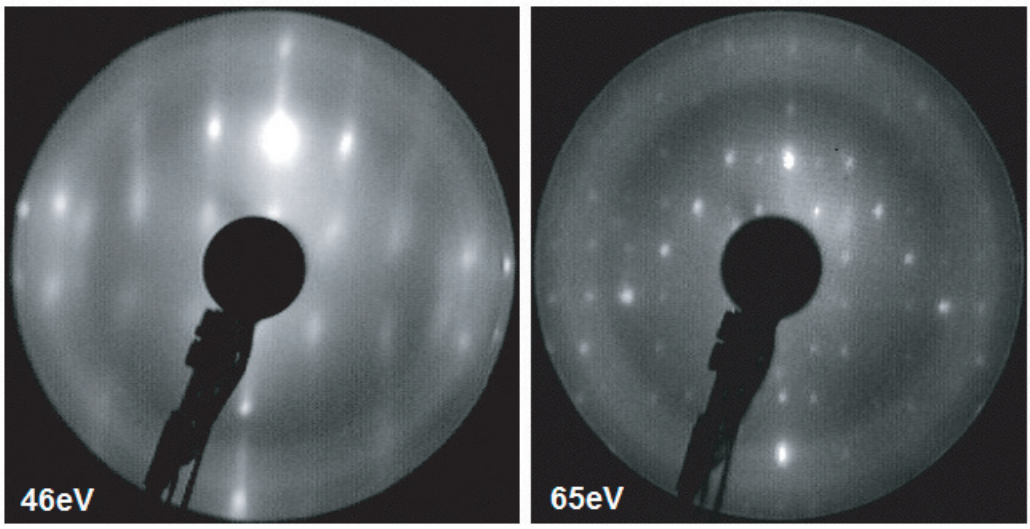

Figure 2.7: Two often seen superstructures after annealing.

amount of CO or other changes.

Over night/weekend the crystal was covered with 6–9 L of oxygen or CO (2–3 min in 5×10^{-8} mbar oxygen pressure at room temperature) (LEED shows that this amount of oxygen or CO at low pressure conserves the step periodicity).

2.4.2 Evaporation of Ni and Post Oxidation

To decorate the Rh surface with Ni atoms, the substrate was held at 420 K and Ni was evaporated (from a rod of 99.98 % purity) [10]. For a submonolayer coverage the rate of evaporation usually was 2–3 min/ML, for a thicker layer $\leq$1 min/ML.
The deposition rate was measured with a quartz microbalance in digits, where 1 digit on the display corresponds to 10^{-8} g/cm^2. The following characteristic has been used to calculate the actual amount of evaporated material: 1 di $\hat{=}$ 1×10^{-8} g/cm^2, and 1 Mol $= 6.022 \times 10^{23}$ atoms. If the number N_{surf} of atoms per cm^2 of the substrate surface is known, a monolayer of the evaporant is equivalent to

$$1\,\mathrm{ML} \,\hat{=}\, \frac{N_{\mathrm{surf}}\,(\mathrm{atoms/cm^2}) \times M\,(g)}{N_A\,(\mathrm{atoms})}. \tag{2.2}$$

With $N_{\mathrm{Rh}(1\,1\,1)} = 1.596 \times 10^{15}\,\mathrm{atoms/cm^2}$, the molar mass of Ni $M_{\mathrm{Ni}} = 58.69\,\mathrm{g}$ and the Avogadro constant being $N_{\mathrm{A}} = 6.022 \times 10^{23}\,\mathrm{atoms}$, one monolayer corresponds to 15.55 digits. Due to the experimental setup the active region of the microbalance was not covered completely by the well focused Ni beam of the evaporator (compare also the picture Fig. 2.3 where the circle of the evaporated material onto the micro balance can be seen). Taking this into account an empirically correction factor of 0.5 has been used.

Oxidizing the surface has been done via post oxidation in 10^{-8}–$10^{-7}\,\mathrm{mbar}$ oxygen pressure and a substrate temperature of 570 K. The oxygen came from a high-purity oxygen bottle and was introduced into the chamber via a gas handling line and a leak valve. The cleanness of the gas (i. e. insignificant amounts of CO) has been checked by mass spectrometer.

2.4.3 Sample Heating

During the experiments both direct and indirect heating have been used. In the case of direct heating the crystal (which had two holes) was suspended directly on Tantalum heating wires and has been heated by applying a current (<14 A). For indirect heating a Tungsten filament (heated with max. 2.2 A) and high voltage (700–1000 V) between crystal and filament were used.
The temperature has been measured via a Chromel-Alumel thermo couple, which was spot welded onto the edge of the crystal. The temperatures in this work are accurate to ±10 K.

Part II

Experimental Part

Chapter 3

Experimental Results

For the band structure measurements it was of interest to measure the photoelectron emission angle-resolved along a certain direction on the surface. Hence the crystal was rotated into the desired orientation with respect to the reference plane of the angle-resolved UPS (which is the horizontal plane). The rotation has been checked by LEED and the accuracy of the rotation is $\pm 1°$. The tilting angle of the crystal (with respect to the manipulator axis) could not be changed in-situ. The reflection of light (coming from the UPS light source) has been observed via a tiny hole through the analyzer, and it has been found to be in the plane of the ARUPS with good accuracy.
The interesting azimuthal angles on the surface are parallel to the steps, which is the $[1\bar{1}0]$ direction, and perpendicular to it, which is the $[\bar{1}\bar{1}2]$ direction.
The incidence angle of the irradiation with respect to the surface normal has been chosen to 60 ° for all UPS measurements, the energy step size 0.05 eV and the dwell time 1 s. In order to get good statistics several scans have been accumulated. All measurements have been done at room temperature.

First, Auger spectroscopy has been applied to establish the cleanliness of the surface, the evaporant, and the oxygen (the latter has been checked by mass spectrometer as well). Fig. 3.1 shows some representative spectra: The top one shows the Rh(5 5 3) surface after dosing 10 L of oxygen, the O KLL Auger peak can be identified at ≈510 eV, the two weaker Auger peaks of oxygen are visible at lower kinetic energy. The middle spectrum shows Rh(5 5 3) after evaporation of 0.2 ML of Ni, where a weak Auger signal of Ni at 60 eV is visible. Adding more Ni (bottom graph), the peak at 60 eV becomes stronger with respect to the Rh signal and the peaks at higher kinetic energy are visible too: The LMM peak at 830 eV (literature: 848 eV) and several peaks in the range of 700–800 eV.

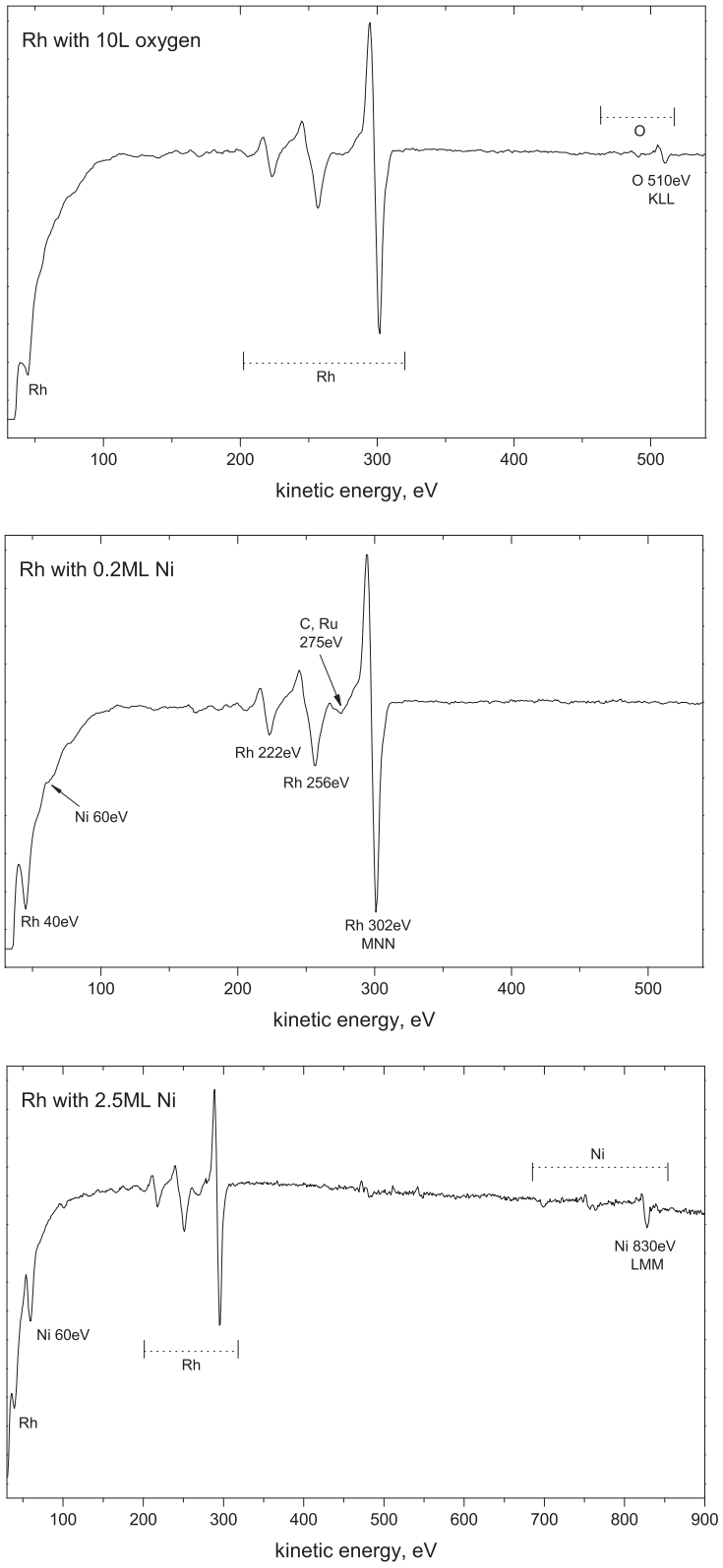

Figure 3.1: AES spectra of Rh(5 5 3) with 10 L of oxygen, Rh with 0.2 ML Ni, and with 2.5 ML, respectively.

3.1 Contamination of Rh(5 5 3) with CO

CO adsorption on metal surfaces is an often studied matter, since the molecule is not only present in the UHV system but also adsorbs within an adequate range of temperature. Due to the large dissociation energy of CO, molecular adsorption is generally observed on metal surfaces, although decomposition of the molecule occurs under certain conditions (substrate temperature, coverage).
When the clean Rh surface is left in UHV, CO adsorbs easily from the ambient gas at room temperature. To prevent the surface from being covered with CO it is flashed to 770 K periodically during long term experiments. CO that adsorbs at room temperature on Rh(1 1 1) does not form the well-ordered (2×2) structure as it does for certain dosages at lower temperature. In order to investigate the adsorption of CO on Rh(5 5 3), and to get a feeling of the degree of contamination of the surface, CO has been dosed at low pressure ($\approx 10^{-8}$ mbar) and room temperature and the surface has been characterized by LEED and UPS. Fig. 3.2 shows some results of the UPS measurements for a dosage of CO of 0.2 L up to 20 L taken at normal emission and 10 ° (measured in the $[1\bar{1}0]$ azimuth, i. e. parallel to the steps), where the bottom curves represent the nearly clean Rh surface. As expected, the adsorption of CO weakens the valence band features of Rh at 0–4 eV binding energy. At the same time the orbitals of CO appear in the spectra at 8 eV and 11 eV, respectively, increasing in intensity with the amount of adsorbed molecules and saturating at ≈10 L. The peaks correspond to the $5\sigma + 1\pi$ (8 eV), and the 4σ (11 eV) orbitals, respectively. The positions of the peaks do not change with coverage.

In Fig. 3.3 the UPS spectra of the CO-covered surface taken at different emission angles are depicted. As it is known for small coverages of CO chemisorbed on metal surfaces, the orbitals show little dispersion (e. g. [21]) typically in the range of 0.2–1 eV. The measurements only cover a fourth of the first Brillouin zone (k = 0 to k = $\pi/2a$) of the substrate and in this region the dispersion of the 5σ and 1π, and 4σ bands is ≈0.13 eV.

The behavior of the UPS spectra is illustrated also by the work function, which is depicted in the bottom graph of Fig. 3.2: Starting with the clean surface at 5.18 eV the course of the work function shows exponential characteristics, it increases rapidly up to 6 eV for ≤4 L of CO and saturates below

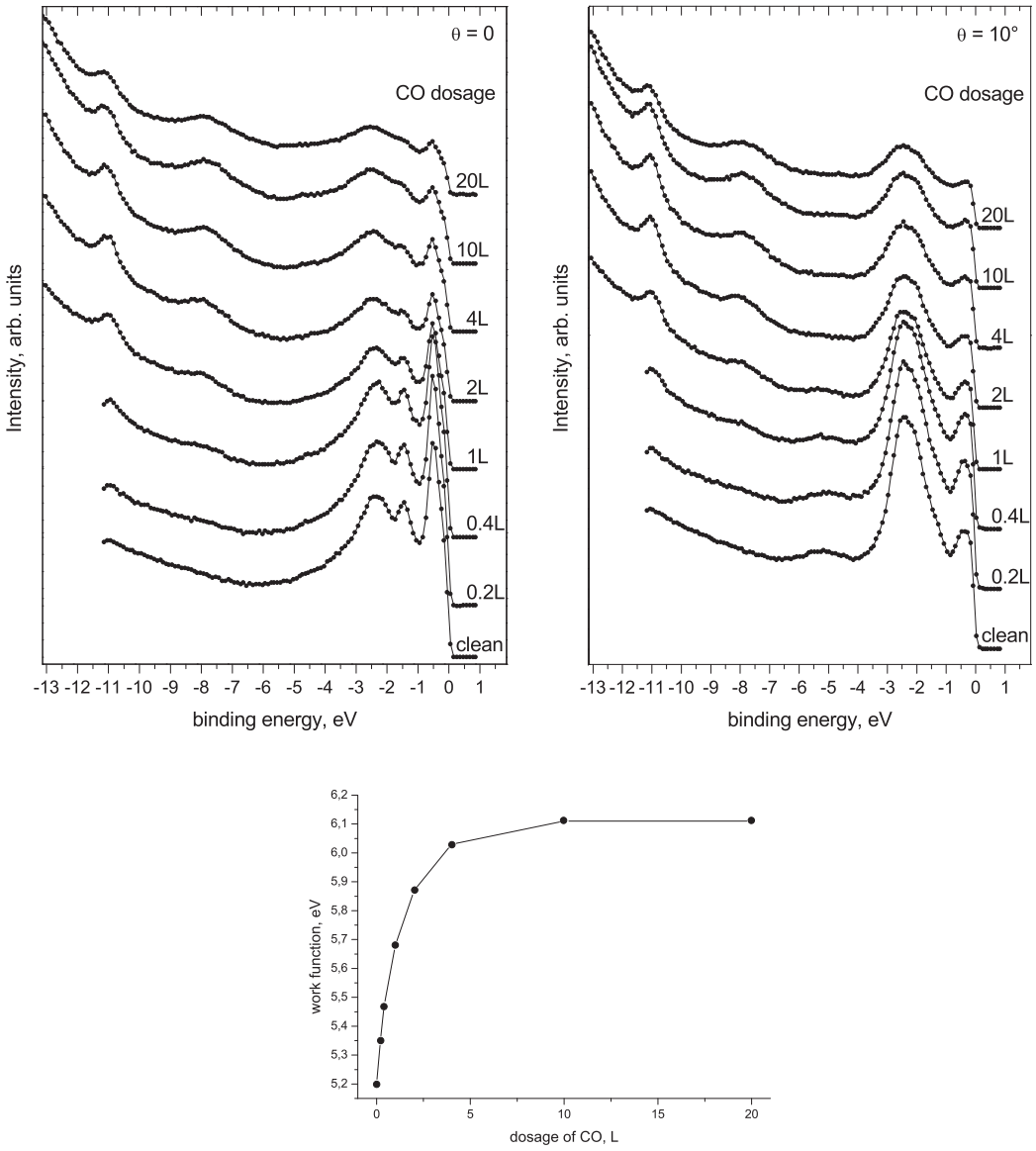

Figure 3.2: UPS spectra for increasing dosages of CO on Rh(5 5 3) measured at normal emission (left) and 10 ° (right). Bottom: Dependence of the work function with increasing amount of CO.

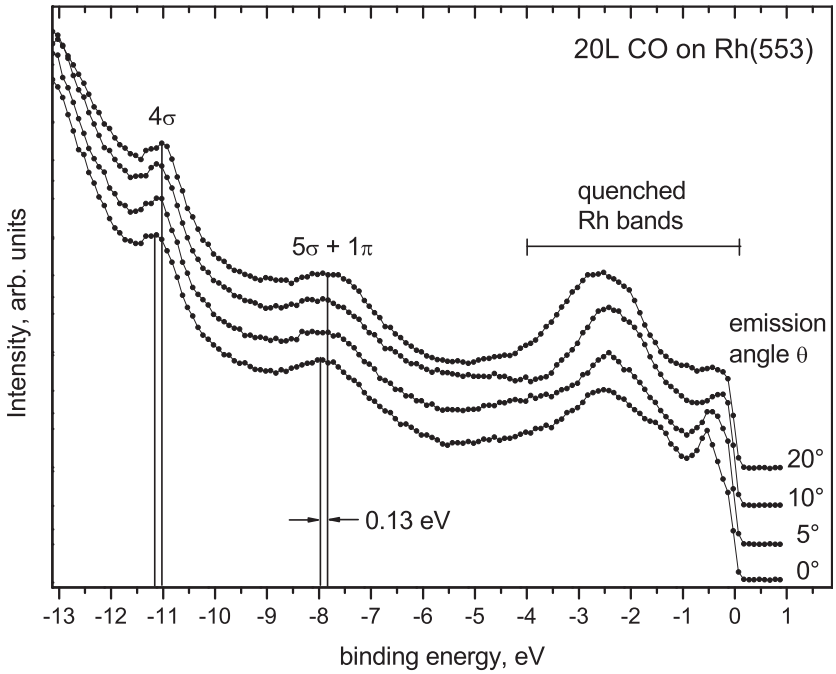

Figure 3.3: Angular dependence of the CO peaks, which disperse toward smaller binding energies.

10 L at 6.11 eV.
The LEED pattern (not shown) shows a sharp spot splitting after dosing 20 L of CO which denotes a well-ordered array of steps and highly blurred additional spots which very likely correspond to a poorly ordered split (2×2) structure [22].

The result of the CO dosing series is that during the band structure measurements the crystal has been flashed after an increase of the work function by <0.1 eV (approximately every two hours). This amount corresponds to ≈0.15 L of CO adsorbed on the surface. It has been checked that this amount of CO does not change the spectra significantly.

3.2 Clean Rh(5 5 3)

3.2.1 Band Structure Measurement Parallel to the Steps

Collections of spectra have been measured by varying the detector angle in steps of 1°. Along the steps the detected emission angle has been covered the range from −40° to 70° (with respect to the surface normal). The Brillouin zone along this direction is given by the nearest neighbor distance of two atoms. This direction on the surface is of interest because the atoms of a step edge form a one-dimensional structure due to the missing of one bond compared to terrace atoms. In an idealized view the whole crystal is an array of one-dimensional structures which are separated by the width of the terraces (≈10.4 Å, or 4.3 rows of atoms). Fig 3.4 shows the measured spectra as a function of the emission angle and kinetic energy for both interesting azimuth directions. The normal emission curves are highlighted with dots. In both sets of spectra the sharp Fermi edge (≈0.3 eV broad at room temperature) can be identified easily at 21.15 eV kinetic energy. Beside this one notices that the spectra parallel to the steps show a symmetry around the normal emission while the spectra perpendicular do not (this matter will be discussed later). Using the left part of equation (1.36) (page 23) allows the conversion of the collections of spectra into intensity band maps with binding energy versus momentum.

The measured band map parallel to the steps is shown in Fig. 3.5 where bright means high intensity, compare with Fig. 3.4. It is symmetric at Γ ($k = 0$) and the boundaries of the first Brillouin zone (its whole width is 2.34 Å^{-1}) are indicated as well. The band structure along the steps contains the interaction of the atoms of the step edge within the chains, and so called 'step states' are formed.
DFT calculations have been performed by the group of F. Mittendorfer of the University of Vienna using the *Vienna ab-initio simulation package* (VASP). Fig. 3.6 shows a DFT calculation of the electronic structure of the surface atoms for a 13 layers slab. The positions of the maxima of the experimental data are indicated as red dots. The calculation fits the data with good agreement: The four peak shape (two sharp next to the Fermi edge, a broad double peak at 2–2.5 eV, and a weak shoulder at 4.5 eV) for small values of k can be identified. In the region around 0.5–1 Å^{-1} and 2–5 eV broad wings of high intensity can be seen in the ARUPS spectra and the calculations show dense states as well. The free electron-like parabola band between the Fermi edge and ≈1 eV binding energy at $k = 0.5$–1 Å^{-1} very likely corresponds to terrace atoms (compare Fig. 3.7). The downwards dispersing band around

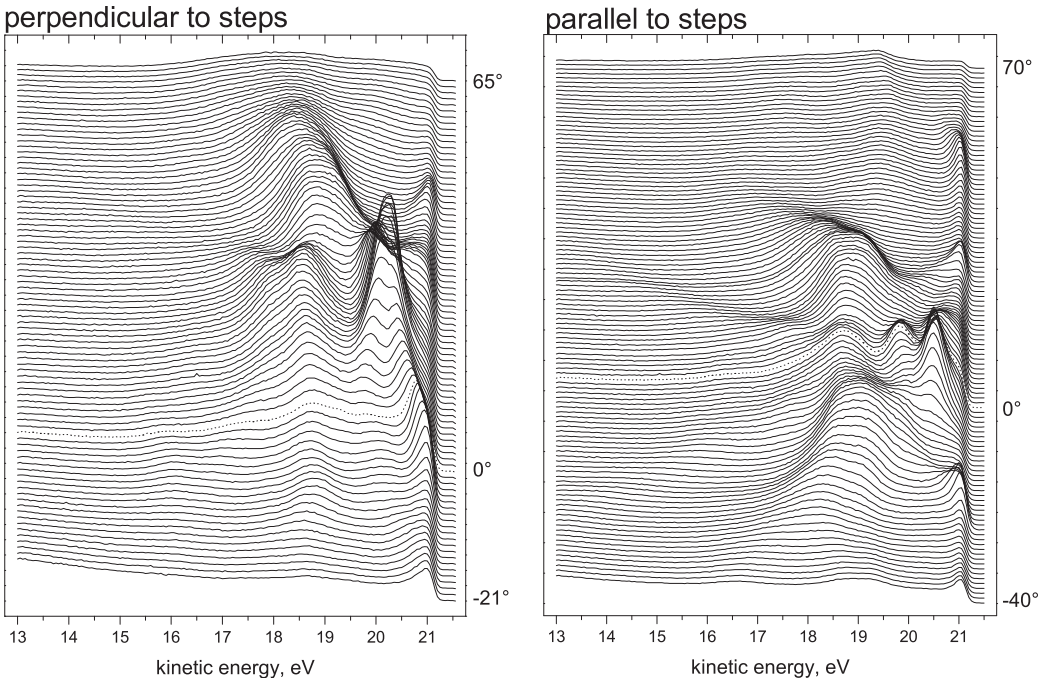

Figure 3.4: Angle-resolved UPS spectra of the band structure measurements of clean Rh(5 5 3) perpendicular and parallel to the step edges.

the gamma point is discussed later.
The plot in Fig. 3.7 has been calculated with a higher degree of localization and distinguishes between the states of terrace atoms (blue dots) and the step atoms (black dots). The maxima of the measurements corresponding to Fig. 3.4 are indicated again (green). It can be seen that most of the step states are close to the states of the surface terrace atoms but shifted to lower binding energies, except the state at 3–3.5 eV close to the first Brillouin zone boundary. Unfortunately the cross-section of the calculated step state between the Fermi edge and ≈2 eV at 0.5–0.8 Å^{-1} and the terrace state around gamma at 5 eV seems to be small since these states cannot be clearly seen in the experimental measurements. Another reason for the weak intensity of some states might be the background of bulk states in the spectra: Calculations of the projected bulk states (not shown here) show a very dense background of states with lots of action in the whole region of the first Brillouin zone between the Fermi edge and 6 eV binding energy. These bulk states actually dominate the measured spectra, and the surface states of terrace and step atoms unfortunately lie right in-between them.

In the measured band map another effect can be seen as well: The strongly downwards dispersing band from the gamma point (BE > 4 eV) can be associated with a secondary electron resonance, which means secondary electrons that are scattered into a preferred final state [23].

3.2.2 Band Structure Perpendicular to the Steps

Perpendicular to the steps along the $[\bar{1}\bar{1}2]$ direction the repeating unit in reciprocal space is small compared to the periodicity in the $[1\bar{1}0]$ azimuth. It is given by the width of the terraces, and the size of the first Brillouin zone is 0.57 Å^{-1}. For this direction a contribution of the emission of the (1 1 1) terraces can be expected in the band structure, see also Fig. 3.9.

The plotted band map is shown in Fig. 3.8, where the gamma point and the boundary of the first Brillouin zone are indicated. The bands do not show any symmetry around gamma since vicinal surfaces have no mirror plane symmetry for the direction perpendicular to the steps.
Comparing the band map with the experimental setup of Fig. 3.9 one understands that the band structure is dominated by the photoemission of the (1 1 1) terraces. The band map has been measured with respect to the (5 5 3) plane, which is the optical plane of the crystal. At the given mounting of the crystal the normal emission of the terraces (which is tilted by 12.3 ° with

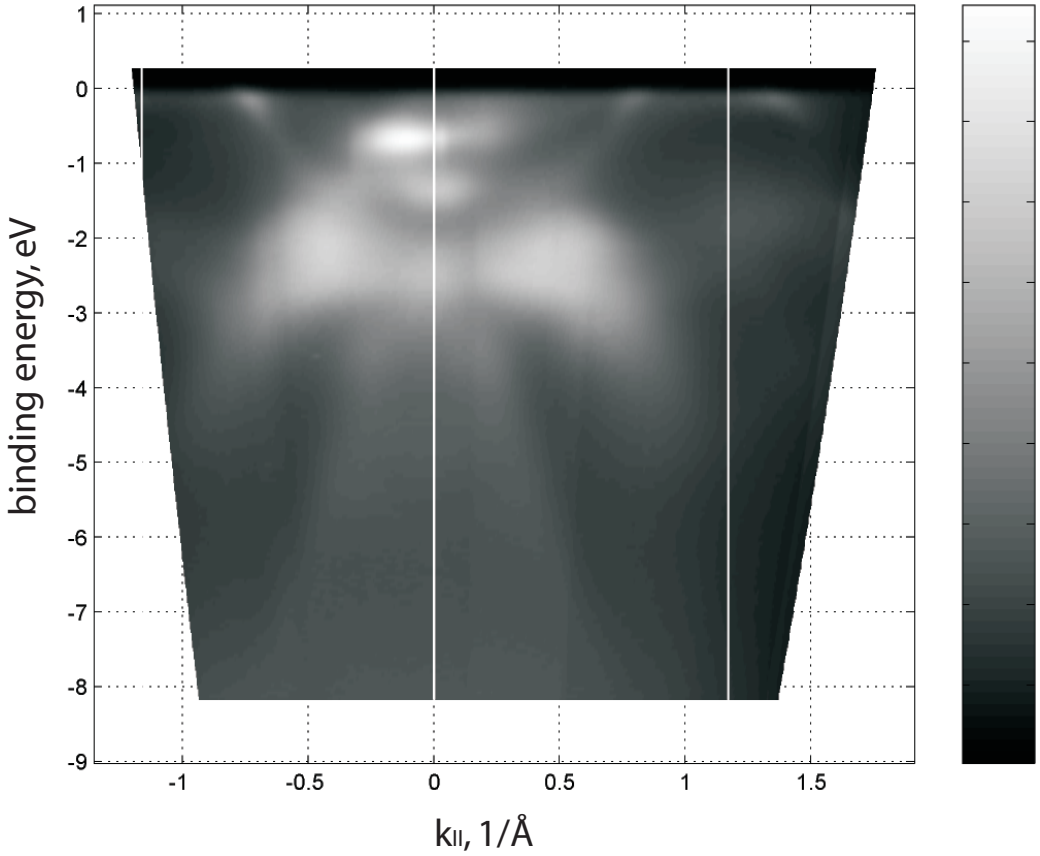

Figure 3.5: Band structure measurement of clean Rh(5 5 3) in the direction along the steps. Gamma point Γ ($k = 0$) and boundaries of the first Brillouin zone ($k = \pm 1.17\,\text{Å}^{-1}$) are indicated. The narrow and strongly downwards dispersing band (BE > 4 eV) is related to a secondary electron resonance and not a feature of the actual valence band.

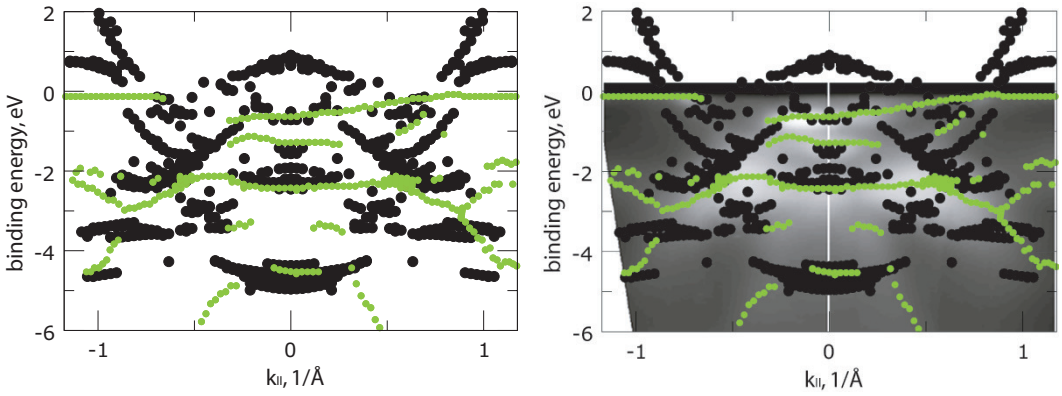

Figure 3.6: Black dots: DFT calculation of the valence band of a Rh(5 5 3) 13 layers slab for a low degree of localization. Green dots: Maxima positions of ARUPS measurements. In the right panel the measured band map has been superimposed on the calculation.

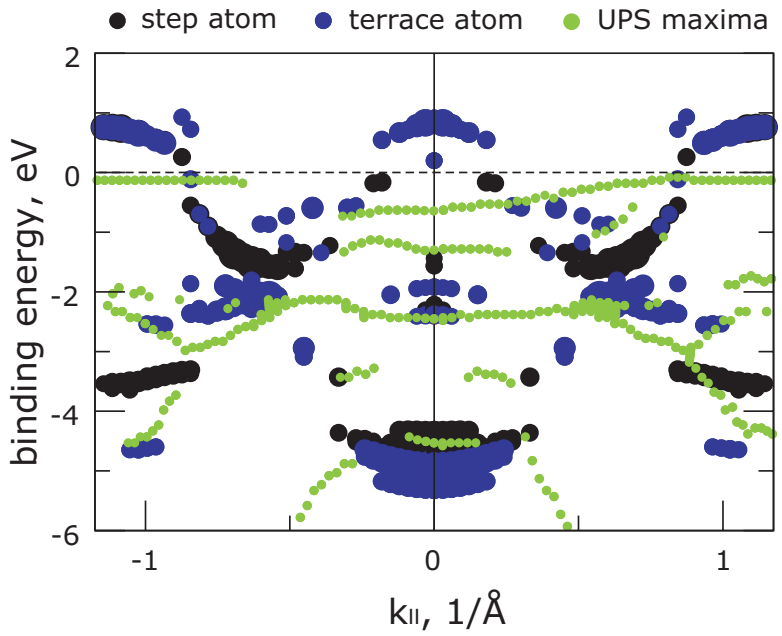

Figure 3.7: DFT calculation of the valence band of Rh(5 5 3) with a higher degree of localization than in Fig. 3.6. The plot distinguishes between the states corresponding to terrace atoms (blue dots) and step atoms (black dots) within the first Brillouin zone. Green dots: Maxima positions of ARUPS measurements.

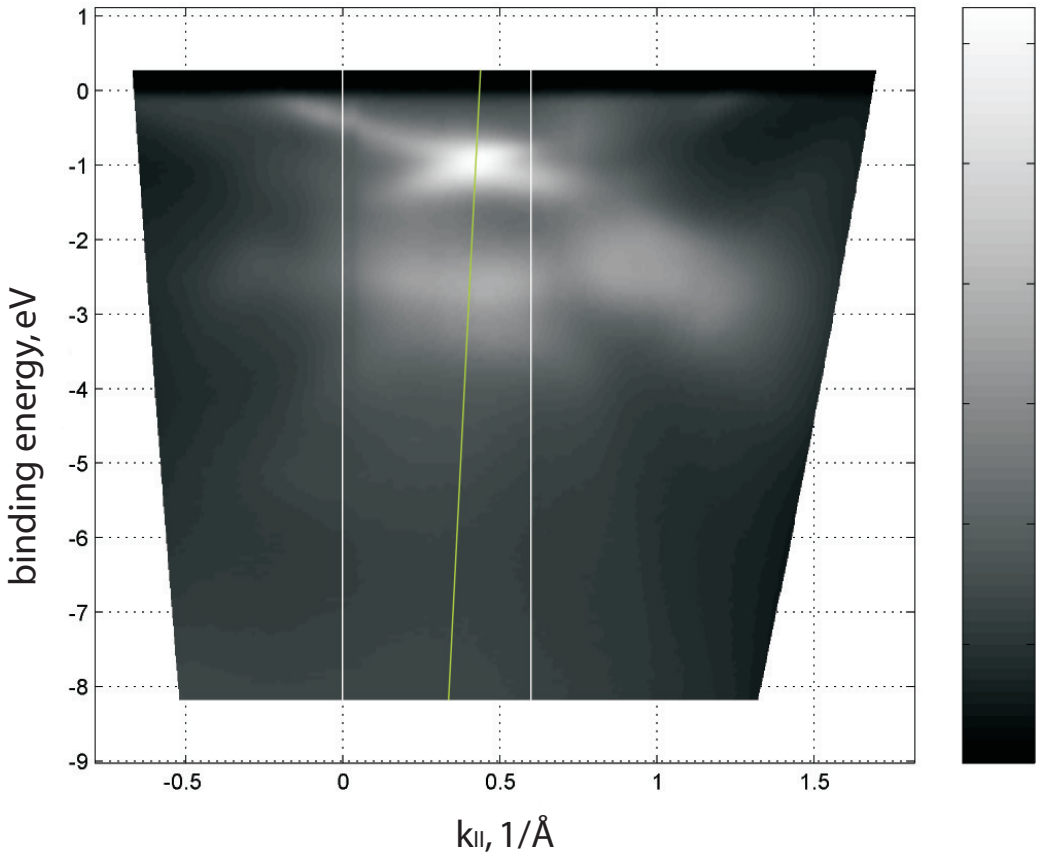

Figure 3.8: Band structure measurement of clean Rh(5 5 3) in the direction perpendicular to the step array. The gamma point ($k = 0$) is indicated, the line at $k = 0.57\,\text{Å}^{-1}$ corresponds to the size of the terraces. Green line: 12° emission spectrum which corresponds to the normal emission of the terraces.

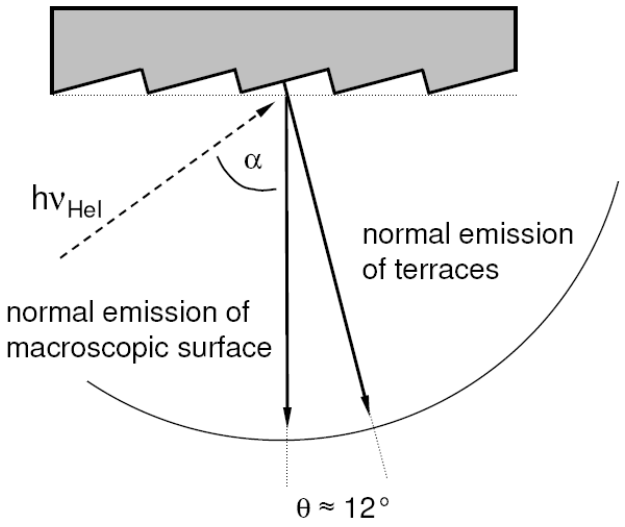

Figure 3.9: Top view of the UPS setup for the measurement perpendicular to the steps. The analyzer is rotated along the circular curve.

respect to the (5 5 3) surface) is shifted toward positive emission angles (with respect to the macroscopic surface normal) and therefore the emission of the terraces is shifted in k-space too. In the band map of Fig. 3.8 the normal emission of the terraces is indicated with the (inclined) green line.

The 12 ° emission spectrum of the Rh(5 5 3) surface can be compared to the normal emission spectrum of a Rh(1 1 1) surface. Both curves are drawn together in Fig. 3.10 where the thin curve is the 12 ° emission and the thick curve the normal emission spectrum (room temperature measurement taken from [23]). It can be seen that the positions of the peaks of both spectra agree perfectly well with each other, not only in energy but also in comparative intensities. In the referred paper the broad peak at 5 eV binding energy of the Rh(1 1 1) spectrum has been related to a secondary electron emission (and not a surface state), which can be identified in the spectra of the vicinal surface as well.

3.3 Oxygen on Rh(5 5 3)

In chapter 3.5 the post-oxidized Ni-decorated surface will be investigated. For reference purposes the clean Rh(5 5 3) has been oxidized as well and

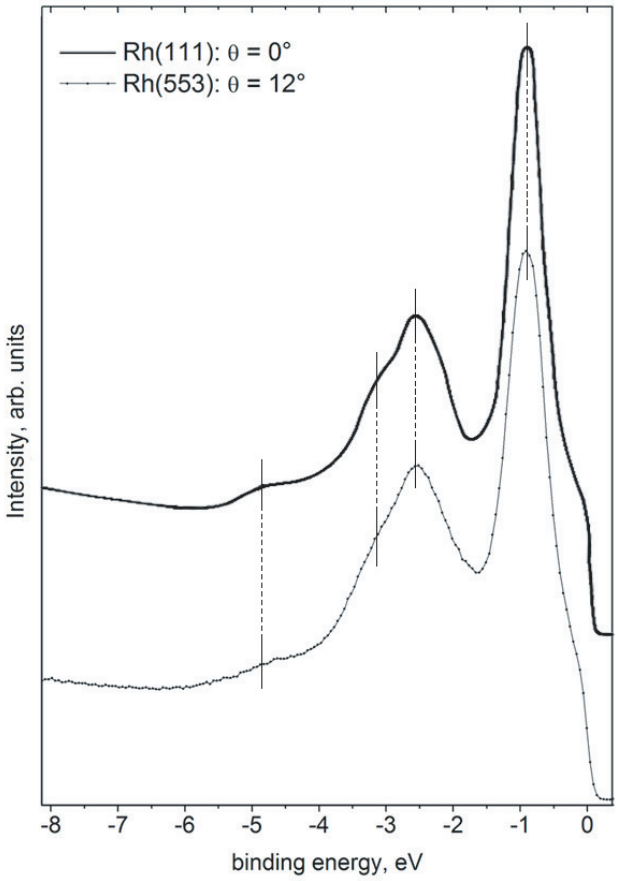

Figure 3.10: Normal emission spectrum of Rh(1 1 1) (thick curve) and 12 ° spectrum of Rh(5 5 3) (thin curve): They agree in peak positions and shape, even the secondary electron peak corresponding to a excitation into a highly free electron like final state of the (1 1 1) terraces is visible.

characterized by UPS and LEED. The substrate temperature has been kept at 570 K during exposure and the oxygen pressure was 10^{-8} mbar for dosages <10 L and 5×10^{-8} mbar for 10 and 20 L. It is known that oxygen at this low pressure does not induce step bunching or faceting but covers the surface with a (2×1) structure with three domains (there is no preferred orientation on a 5 atoms wide terrace) [8].
In the valence band spectra the changes due to the adsorption of oxygen are very small. The position of the O 2p-orbitals are indicated with dotted lines in Fig. 3.11 at higher oxygen dosages in the range of 5.5–6.6 eV binding energy. The shape of the Rh 4d features does not change dramatically with increasing amount of oxygen: The band at 1.5 eV does not weaken in intensity nor shows it any shifting in energy, the bands at 0.5 eV and ≈2.5 eV decrease slightly in intensity and the former shows a small shift by 0.1 eV to higher binding energies. A LEED pattern with the characteristic (2×1) structure with three domains after exposing the surface to 20 L of oxygen is depicted in Fig. 3.12. The splitting of the spots due to the arrangement of the steps is still clearly visible.

3.4 Nickel on Rh(5 5 3)

In this section, the decoration of the Rh surface with Ni atoms is discussed. For a small coverage (<1 ML) the growth of Ni is known to be pseudomorphous and the Ni atoms are attached to the step edges and grow line-by-line. When the growth of Ni on Rh(5 5 3) is studied by valence band spectroscopy, one sees that the photoemission signal of the Ni 3d bands increases in intensity (with respect to the Rh 4d signal of the (5 5 3) surface) for coverages in the sub-monolayer regime, reaches a maximum of intensity for 0.2 ML Ni and decreases for higher coverages (even several ML thick films). This behavior has not been found only for a photon energy of $h\nu = 21.21$ eV, which has been used for the experiments of this work, but also for $h\nu = 110$ eV (synchrotron radiation), where the photoemission cross-section of Rh in minimal.

3.4.1 Step Decoration with 0.2 ML Ni

At a coverage of 0.2 ML Ni the step edges of the Rh(5 5 3) surface are fully decorated with one-dimensional chains. The direction of the angle-resolved measurement is therefore along the steps and the interest is focused on the interaction of Ni atoms within the 1D chains and the resulting dispersion of

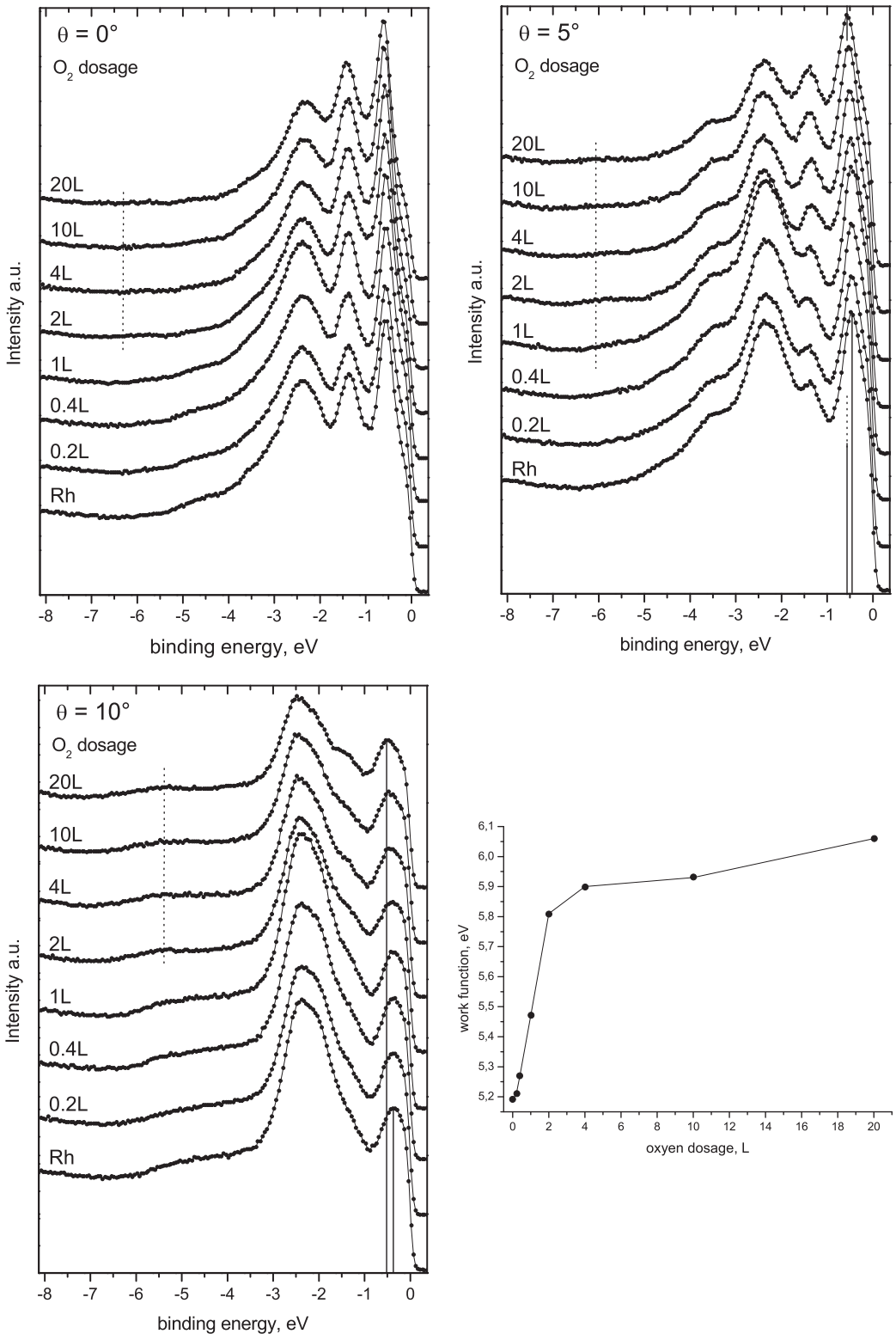

Figure 3.11: Normal emission, 5°, and 10° valence band spectra of clean Rh(5 5 3) and after dosing oxygen up to 20 L (at a substrate temperature of 570 K). Bottom right: Evolution of the work function with increasing dosage of oxygen.

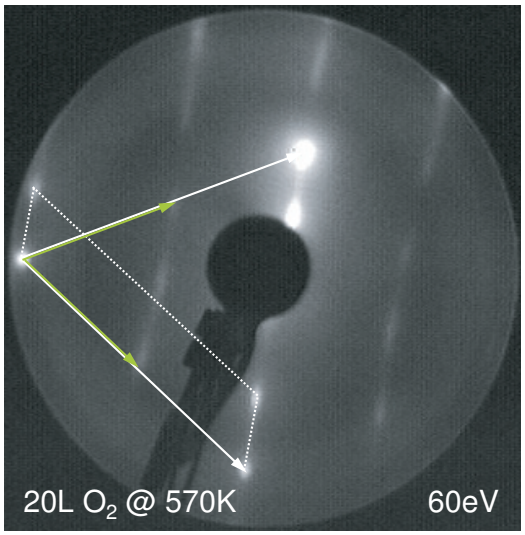

Figure 3.12: LEED pattern of Rh(5 5 3) with 20 L of oxygen dosed at 570 K substrate temperature. The vectors of the unit cell of the (1 1 1) terraces (solid white), the (2×2) pattern (solid green), and the unit cell of the step array (dotted) are indicated.

the Ni bands.
The work function of Rh(5 5 3) decorated with 0.2 ML Ni is 5.09 eV.

Since the changes in the UPS spectra (photon energy $h\nu = 21.21$ eV) due to addition of Ni are very small, both the spectra of the clean Rh(5 5 3) and the Ni-decorated Rh(5 5 3) have been measured consecutively for several emission angles, and the difference curves of these spectra have been calculated (Ni-decorated Rh(5 5 3) minus clean Rh(5 5 3)). A collection of these results is shown in Fig. 3.13. The solid circles are from bare Rh and the curves with the open circles are Ni-decorated Rh, both plotted on the same intensity scale. The difference curves (thin solid) are displayed with equal magnificent intensity, the zero value corresponding to them is indicated.

DFT calculations for the Rh(5 5 3) surface with Ni-decorated steps have been performed again by the group of F. Mittendorfer, and are depicted in Fig. 3.14. The lines in the right half of the band map correspond to the positions of the measured spectra of Fig. 3.13 in k-space.
The calculation shows two very flat Ni derived bands: For small values of momentum one band is around 0.5 eV and the other one at 1.6 eV with respect to the Fermi edge. The band close to the Fermi edge does not show any

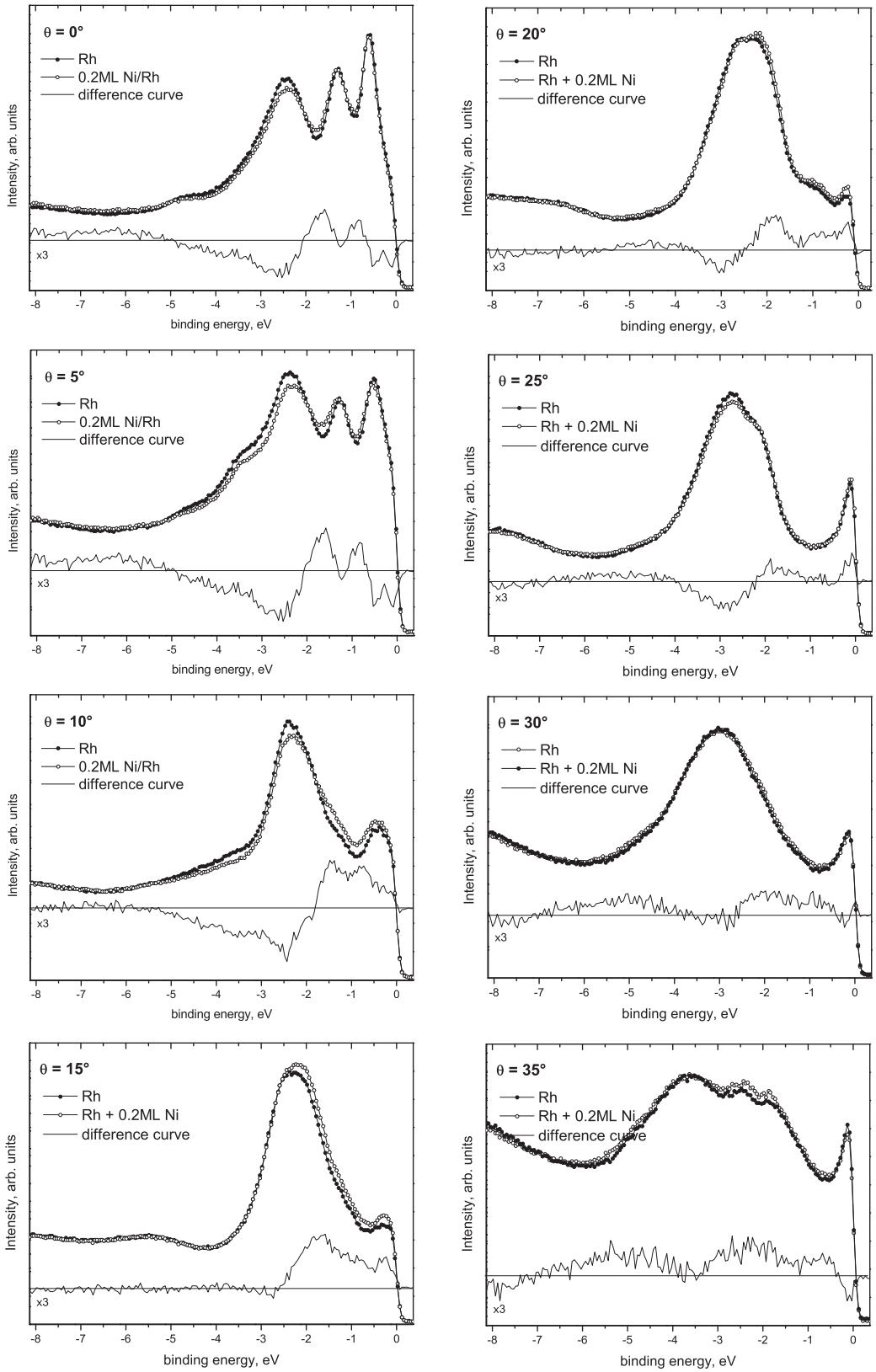

Figure 3.13: UPS spectra of different emission angles for 0.2 ML Ni on Rh(5 5 3). The difference curves are the Rh + 0.2 ML Ni spectra minus the clean Rh spectra.

dispersion for $k < 0.8\,\text{Å}^{-1}$, the band at 1.6 eV runs up to 1 eV at $k \approx 0.3\,\text{Å}^{-1}$ and there it remains. Coming closer to the Brillouin zone boundary both bands finally run up a bit more to the Fermi edge; the upper band cuts it at k $\approx 1\,\text{Å}^{-1}$ while the band below shows very weak dispersion in this range and remains at 0.6 eV.

The DFT calculation fits the measured spectra qualitatively very well, where two bands between the Fermi edge and -2 eV are found (see difference spectra of Fig. 3.13). They show no dispersion for small values of k, but coming closer to the first Brillouin zone boundary one notices the upper band running up to the Fermi edge.
The dispersion of the bands is roughly 0.7–1 eV and one could ask why they do not disperse much more. The answer can be found in the fact that the growth of Ni on Rh is pseudomorphous: The Ni atoms adopt the same lattice geometry as Rh. DFT calculations for 0.1 and 0.2 ML of Ni have shown that the highest adsorption energy for Ni on Rh(5 5 3) at the lower step edges in fcc-facet sites. The bridge site between two step atoms is the most unfavorable adsorption site. The distance between two Ni atoms along the steps is the Rh lattice constant. Since Ni atoms are smaller than Rh atoms and because of their distant sites they have little overlap and therefore flat bands. Ni has to expand by 9 % (with respect to its own lattice constant) to adopt the Rh lattice constant.
The present measurement and DFT calculations agree with previous synchrotron measurements: There, valence band spectra have been measured at the energy of the Cooper minimum of Rh (110 eV) and they yielded an increase of intensity between the Fermi edge and 2 eV after evaporation of Ni. The effect of increasing intensity is of course much weaker using the energy of the He I radiation, but on the other hand the low energy allows a high resolution in k space which is necessary for the determination of the band structure.
DFT calculations of the contribution of the atoms right at the surface to the density of states are published in [11]. After Ni decoration the photoemission of the Ni 3d stated dominates and is located between the Fermi edge and 2 eV binding energy. The calculation shows again that the d-orbitals of Ni are much more localized than the d-orbitals of Rh, as it can be seen in the UPS spectra as well.

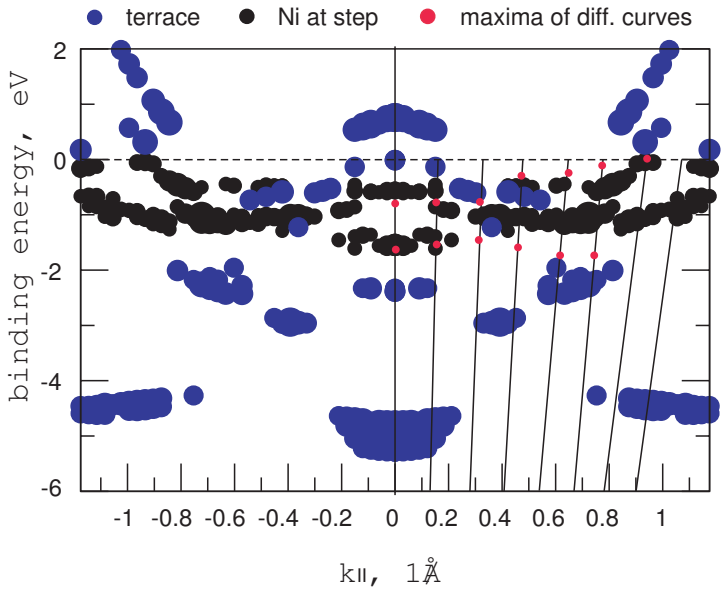

Figure 3.14: DFT calculation of the valence band parallel to the steps, for a step decoration of 0.2 ML Ni. The black dots correspond to the Ni decoration, the blue dots represent the terrace states, and the red dots indicate the maxima positions of the experimental data (difference curves).

3.4.2 Step Decoration with 0.4 ML Ni

When the Ni coverage is doubled to 0.4 ML, the steps are decorated with two rows of Ni atoms (in the ideal case). Therefore the surface has been cleaned, checked by UPS (especially the work function, which is the most surface-sensitive measured variable, which is available with the equipment of the UHV system), and 0.4 ML of Ni have been evaporated onto the heated substrate.

Angle-resolved valence band measurements for different emission angles are plotted in Fig. 3.15. The photoemission intensity of the Ni-decorated Rh(5 5 3) surface, which increased for the coverage of 0.2 ML Ni (with respect to the Rh(5 5 3)), decreases when the coverage is doubled to 0.4 ML Ni. The difference curves (thin solid lines) behave similar as those of the step decoration with 0.2 ML Ni and fit well into the pattern observed for the growth of Ni on Rh(5 5 3) (see next chapter). The two bands at 1 eV and 1.7 eV (maxima in the difference spectra) are clearly visible in the normal emission and 5 ° valence band spectra. For $\theta = 10\,^\circ$ the band at higher binding energy moves slightly towards the Fermi edge. At larger emission angles the bands cannot be separated any more. The characteristic decrease in intensity of the peak at 2.5 eV (in the normal emission spectra), which happens when the surface is covered with adsorbates (adsorbed or evaporated), can bee seen very well: The minimum of the decrease follows the peak at 2.5 eV of the Rh 4d bands in energy and disperses about 1 eV (in the first Brillouin zone). Comparing this with the DFT calculation, illustrated in Fig. 3.16, the minima can be related to terrace and step states of Rh(5 5 3), which are quenched now.

3.4.3 Growth of Nickel on Rh(5 5 3)

As mentioned above, a low coverage of Ni atoms evaporated onto the heated Rh(5 5 3) substrate decorates the steps and produces atomic rows along them (monoatomic rows at a coverage of 0.2 ML). The growth is pseudomorphous and one does not see any new structures in the LEED. Fig. 3.17 shows diffraction pattern for different coverages of Ni on Rh(5 5 3): Increasing the coverage from the sub-monolayer range to 1 ML the LEED pattern does not show any changes with respect to the clean Rh(5 5 3) surface, which suggests that Ni grows on the terraces by forming a (1×1) structure, and the step morphology is maintained. Even doubling the coverage to 2 ML of Ni does not produce any changes of the diffraction pattern. Increasing the thickness

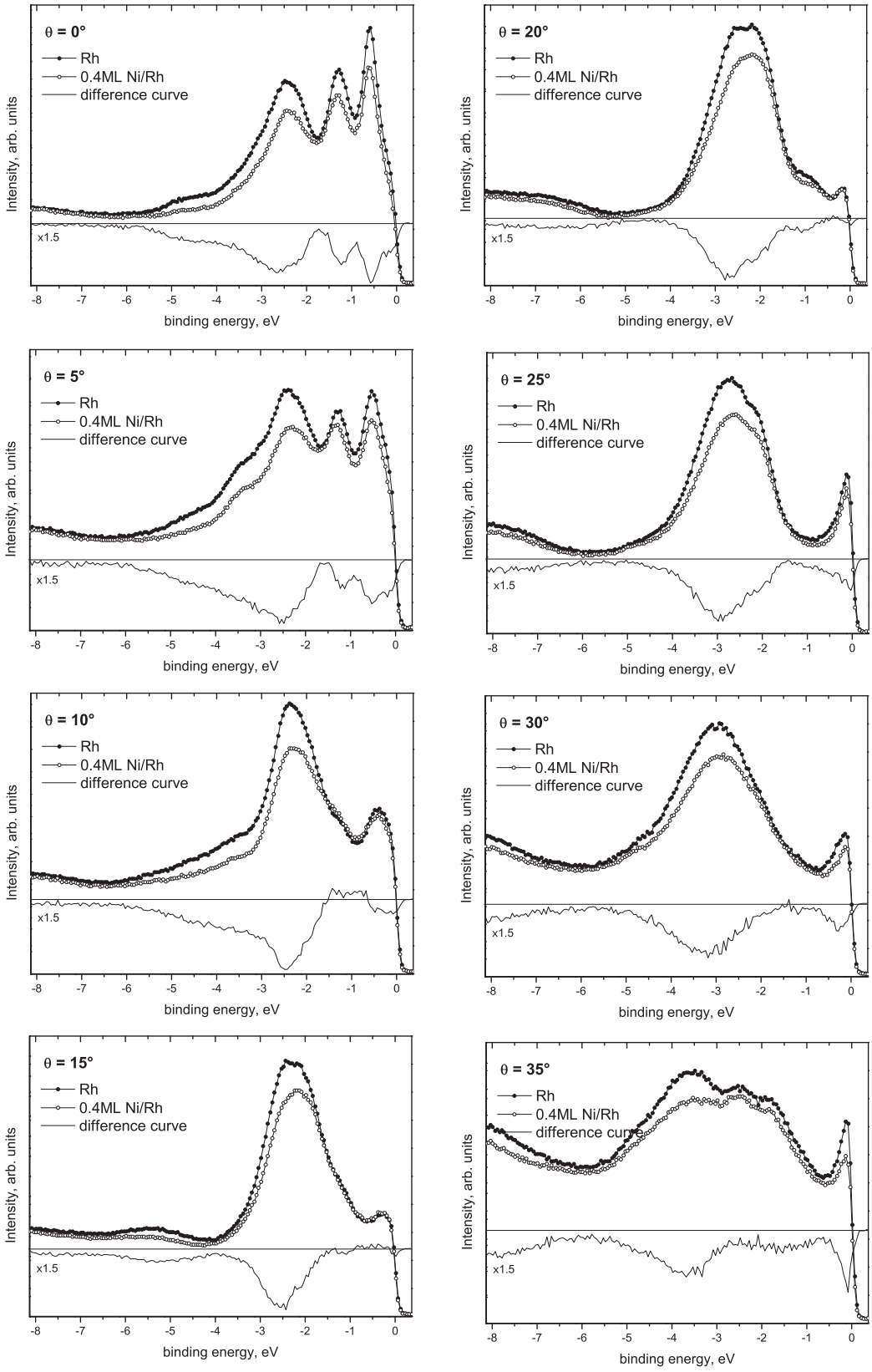

Figure 3.15: UPS spectra of different emission angles for 0.4 ML Ni on Rh(5 5 3). The difference curves are the Rh + 0.4 ML Ni spectra minus the Rh spectra.

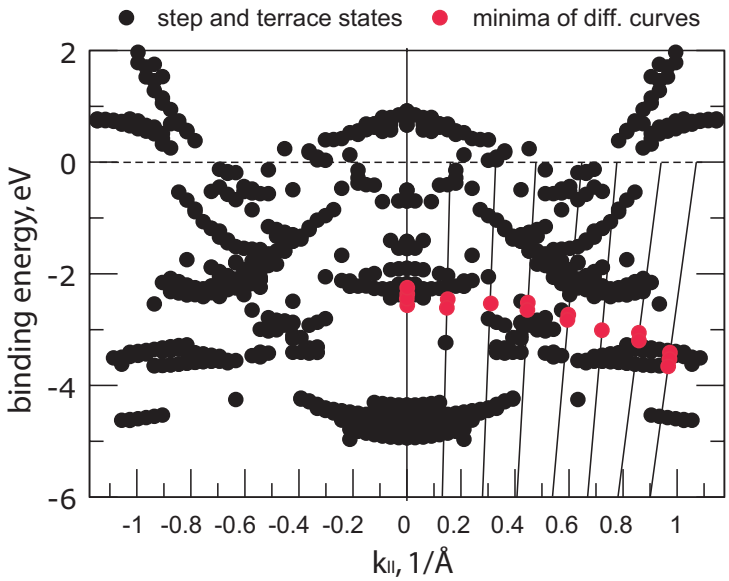

Figure 3.16: DFT calculation of the valence band of the 13-layer Rh(5 5 3) slab for a low degree of localization. For the correlation with terrace and step states see Fig. 3.7. Red dots are the minima of the difference spectra, which correspond to quenched Rh 4d states.

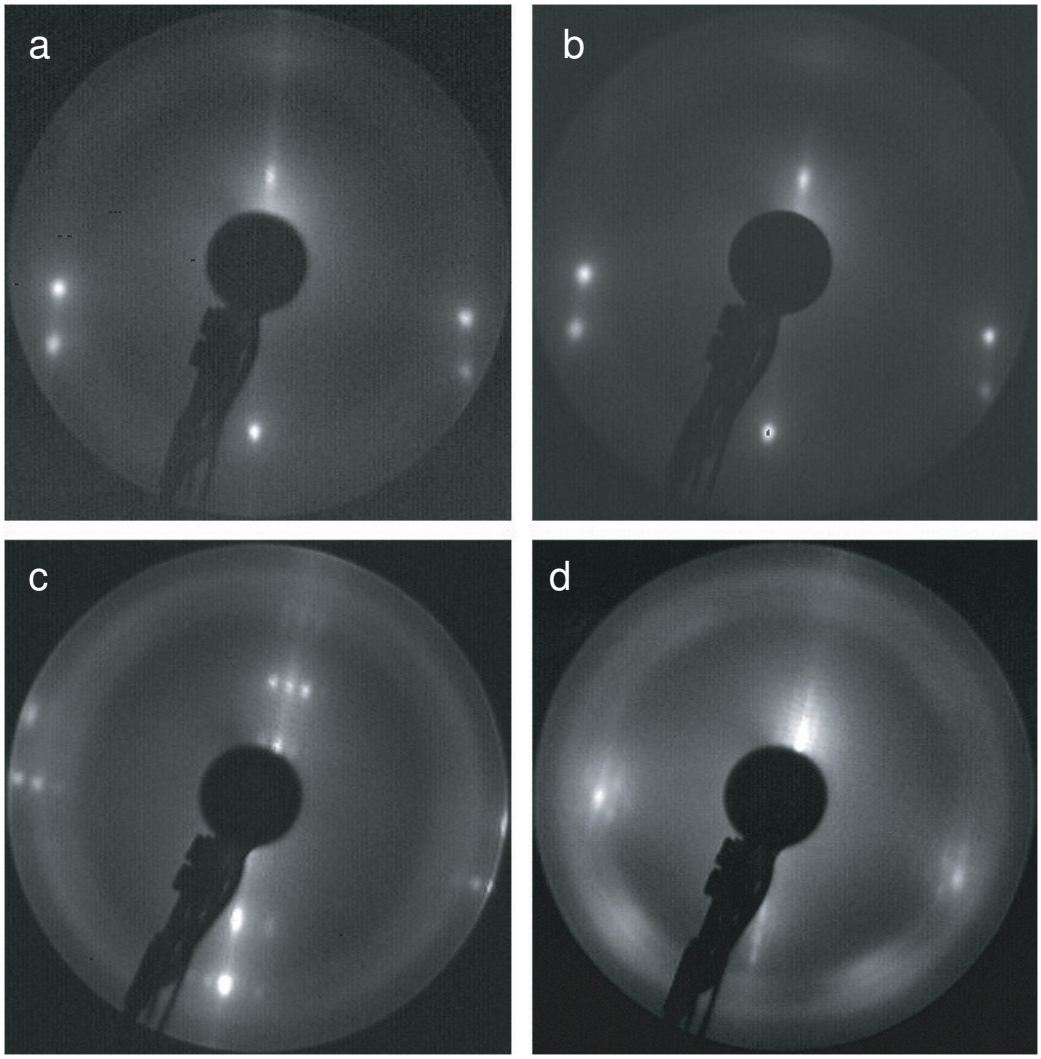

Figure 3.17: LEED pattern for different coverages of Ni on Rh(5 5 3): (a) 0.8 ML (88 eV) no changes with respect to clean Rh(5 5 3), (b) 2 ML (88 eV) like (a), (c) 5 ML (63 eV) narrow split spots due to faceting, and (d) 10 ML (120 eV) hexagonal moiré structure.

of the Ni layer up to of 5–6 ML, the array of well ordered steps still exists with the terrace width of the Rh(5 5 3) substrate. Beside that, the film forms large facets (or a reconstruction along the steps?), whose appearance in the diffraction pattern are additional spots perpendicular to the step direction. The periodicity of the sharp and narrow spots is ≈20 times the atomic distance. Increasing the coverage to 10 ML the surface of the Ni film becomes completely independent of the step morphology of the Rh(5 5 3) substrate and forms a hexagonal moiré structure.

Although the global symmetry of the surface changes for thicker layers of Ni, the valence band does not show any unexpected behavior. In Fig. 3.18 representative valence band spectra of the growth of Ni on Rh(5 5 3) of several emission angles are depicted, where the bottom curves represent the valence band of the clean Rh(5 5 3) surface for each emission angle (with respect to the surface normal). The Rh 4d bands are more and more quenched in intensity by increasing the Ni coverage, especially the peaks labeled as (1) and (3) at 0.6 eV and 2.4 eV, respectively. Both show small shifts (indicated only in the normal emission spectra), which are distinct (with respect to the respective smaller coverage) when the monolayer and the moiré structure are formed, respectively. The peak (2) at 1.4 eV of the valence band (in the panels for $\theta = -5°$, $0°$, and $5°$) changes less, which is also illustrated in Fig. 3.19: In the difference curves (Ni covered Rh(5 5 3) minus clean Rh(5 5 3); the peaks of Fig. 3.18 correspond to minima now) of the normal emission spectra the slow decrease of (2) with respect to (1) and (3) can be clearly identified. The reason are the two bands (a) and (b) (1 eV and 1.7 eV, respectively), which are associated to the presence of Ni on the surface. Both bands remain constant in binding energy and for coverages higher than 1 ML even in intensity (the latter with respect to the clean Rh(5 5 3) spectra).
The Rh secondary electron resonance, which causes e. g. the broad shoulder at 5 eV in the 10 ° valence band spectra, vanishes after covering the surface with 2 ML of Ni. Some of the spectra, which are shown in Fig. 3.18, are plotted in a different way also in Fig. 3.27, where the absence of the resonance is better visible.

The behavior of the work function is depicted in Fig. 3.20: For clean Rh(5 5 3) it is 5.18 ± 0.01 eV. The work function of clean Rh(1 1 1) has been experimentally found to be 5.6 eV by [24]. A decrease of the work function when a surface creates steps can be expected because dipoles are formed at the step edges.
Increasing the coverage of Ni up to roughly 2 ML the work function decreases about 0.3 eV and passes through a minimum. The addition of more Ni in-

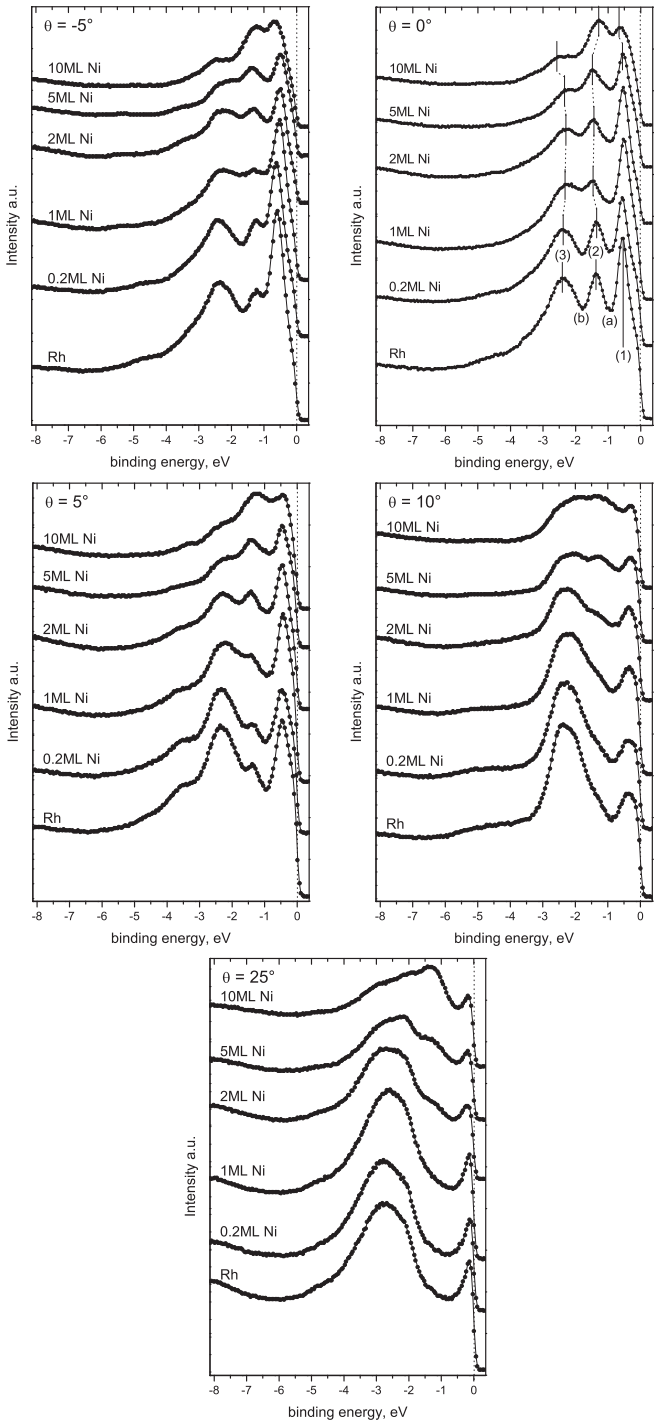

Figure 3.18: Valence band spectra of various emission angles of the growth of Ni on Rh, measured parallel to the steps. The bottom curves are the clean Rh spectra and the coverage increases up to 10 ML, according to the microbalance.

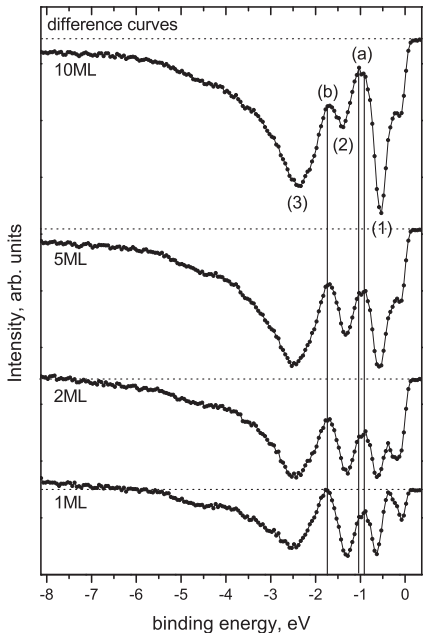

Figure 3.19: Difference spectra (Ni covered Rh(5 5 3) minus clean Rh(5 5 3)) of the normal emission valence band spectra of Fig. 3.18.

creases the work function to 5.2 eV, probably due to relaxation of the topmost layers and therefore a denser surface. There is no saturation noticeable for the work function of a <10 ML thick Ni layer on Rh(5 5 3), a behavior which can be seen in the UPS spectra as well. Anyway, this value is comparable to the work function of Ni(1 1 1), which has been found to be in the range of 5.15 ± 0.10 eV to 5.25 eV ([25] and [26], respectively).

3.5 Oxidation of Ni on Rh(5 5 3)

In this section, the Ni-decorated step edges of the Rh(5 5 3) surface have been post-oxidized with small amounts of oxygen. The oxidation process of Ni-decorated stepped Rh surfaces has been previously investigated by core level spectroscopy and DFT calculations [9]. As written there the formation of Ni-Rh nanostructures increases the adsorption energy of oxygen and the energetically favored sites along the step edges of clean Rh become even more attractive in the presence of Ni atoms attached to them. One can expect that the Ni atoms are oxidized first, while the Rh terraces are covered afterwards. After oxidizing (mainly) the Ni atoms along the step edges, the oxygen dosage

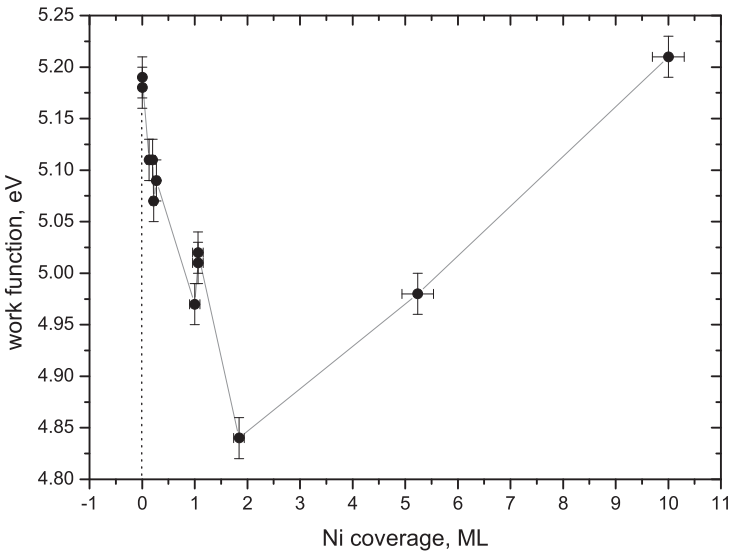

Figure 3.20: Behavior of the work function for the growth of Ni on Rh(5 5 3).

has been increased until the terraces were covered with oxygen as well and a saturation (i. e. of the work function) has been reached. Beside that, higher Ni coverages (at least their surfaces), which have been investigated in chapter 3.4.3, have been oxidized.

3.5.1 Oxidation of 0.2 ML Ni

After evaporation of 0.2 ML Ni the surface has been post-oxidized with 0.2 L of oxygen (in 10^{-8} mbar oxygen pressure) at elevated temperature. This amount of oxygen is sufficient to oxidize the Ni atoms only and the LEED shows that there is no (or at least not much) oxygen on the terraces (oxygen on the Rh(1 1 1) terraces forms a (2×1) structure).
Valence band measurements with synchrotron radiation of the oxidized Ni-decorated Rh(5 5 3) surface indicate a decrease of intensity of the Ni bands and the O 2p state is observed. In the UPS spectra one sees the same. In Fig. 3.21 a series of angle-resolved valence band spectra of the oxidized Ni step decoration on Rh(5 5 3) is depicted: The curves with open circles are the Ni-O/Rh spectra, the solid dotted curves the Ni/Rh spectra, and the difference spectra (Ni-O/Rh minus Ni/Rh) are the thin solid lines. The O 2p band is in the range of 5–6 eV binding energy, but it is hardly visible for this small amount of oxygen, a behavior, which was expected since the Rh(5 5 3)

photoemission signal still dominates the spectra and oxygen gives a weak peak on clean Rh(5 5 3) as well (compare chapter 3.3). In the region of the Ni bands a decrease of intensity and a rearrangement of the Ni (and Rh) states due to hybridization of the O 2p with Ni 3d (and Rh 4d) orbitals can be seen, especially for small emission angles.

This rearrangement of Rh 4d and Ni 3d states is more explicit when the Ni chains are completely oxidized, which happens when the dosage of oxygen is roughly doubled: After oxidation with 0.5 L of oxygen (in 10^{-8} mbar oxygen pressure) at 570 K a hint of the oxygen (2×1) superstructure with three domains on the terraces is discovered with LEED. The angle-resolved measurements for the same emission angles as in Fig. 3.21 are plotted in Fig. 3.22. Due to the hybridization of O 2p orbitals with Ni 3d and also Rh 4d the Ni and Rh states change more explicitly, but the shape of the difference curves is still very similar to the spectra after the oxidation with 0.2 L (except for the valence band spectra taken at normal emission).
At this dosage of oxygen the O 2p band becomes visible at $\approx$5.7 eV.

The work function of the surface oxidized with 0.2 L and 0.5 L, respectively, has been measured as well: After the first oxidation by 0.2 L the increase was 0.26 eV (from 5.09 eV to 5.35 eV), and after the oxidation by 0.5 L of oxygen 0.42 eV (from 5.09 eV to 5.51 eV).

In a further experiment the Rh(5 5 3) surface has been prepared once more with 0.2 ML of Ni and the amount of oxygen has been increased stepwise up to 10 L (10^{-8} mbar oxygen pressure for dosages $<$4 L and 5×10^{-8} mbar for higher dosages, always at elevated temperature). UPS spectra for different emission angles, work function measurements, and the diffraction patterns have been recorded.
The work function measurements, summarized and plotted in Fig. 3.23, resulted in a nearly exponential characteristics with increasing the oxygen dosage. The figure shows the behavior during the whole experiment, starting with the clean Rh(5 5 3) surface at 5.18 eV. After evaporation of Ni the work function decreases slightly to 5.09 eV, and increases rapidly when the surface is oxidized. At the dosage of 10 L of oxygen, where the LEED pattern showed a not very well ordered (2×2) structure of oxygen on the Rh(1 1 1) terraces, the work function has increased by 1.08 eV (with respect to the Ni-decorated Rh (5 5 3) surface) up to 6.17 eV and seems to saturate soon.

A collection of valence band spectra for representative emission angles is depicted in Fig. 3.24. At first view, the evolution of the valence band when

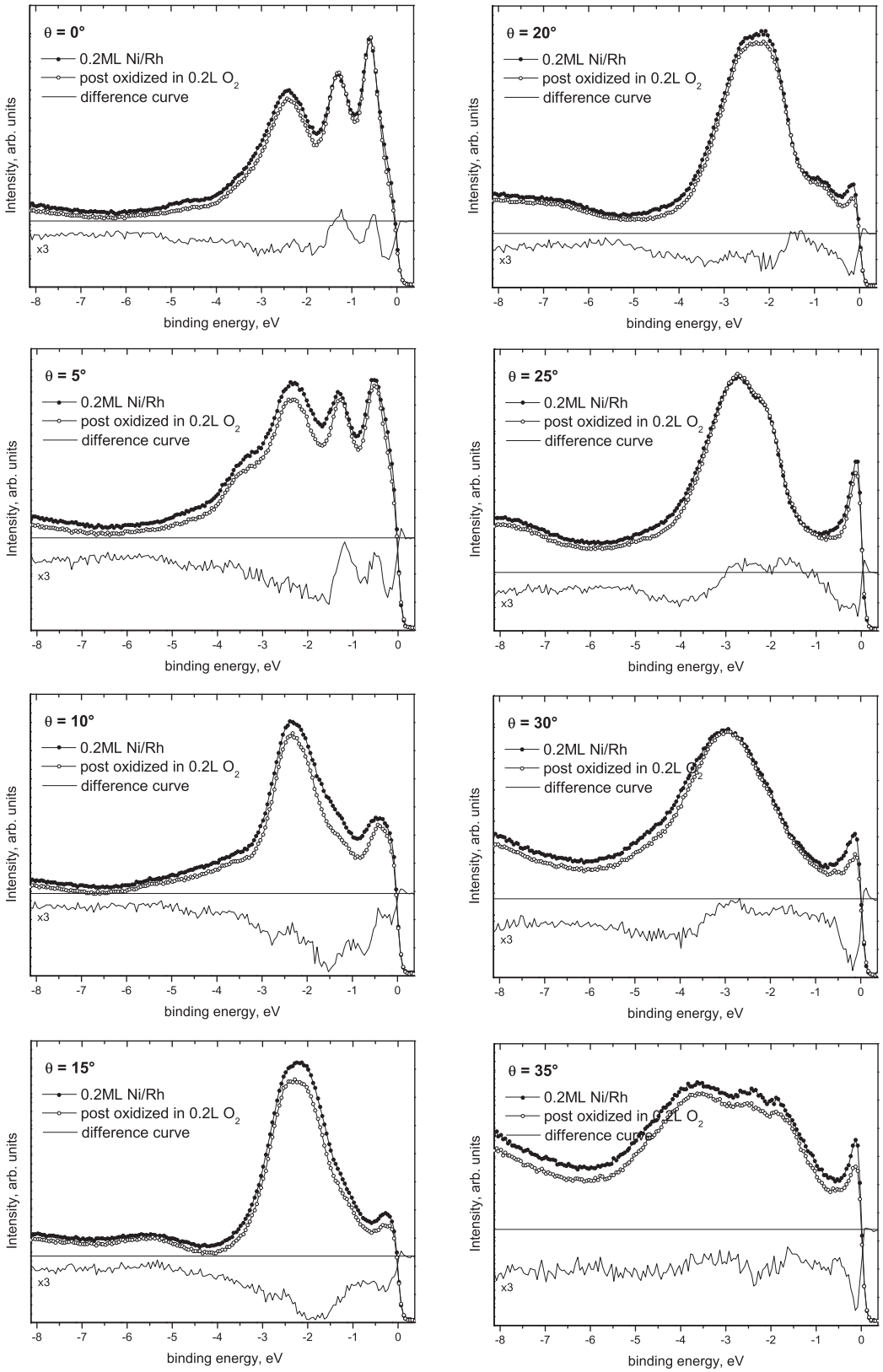

Figure 3.21: UPS spectra of 0.2 ML Ni, oxidized by ≈0.2 L oxygen, for various emission angles.

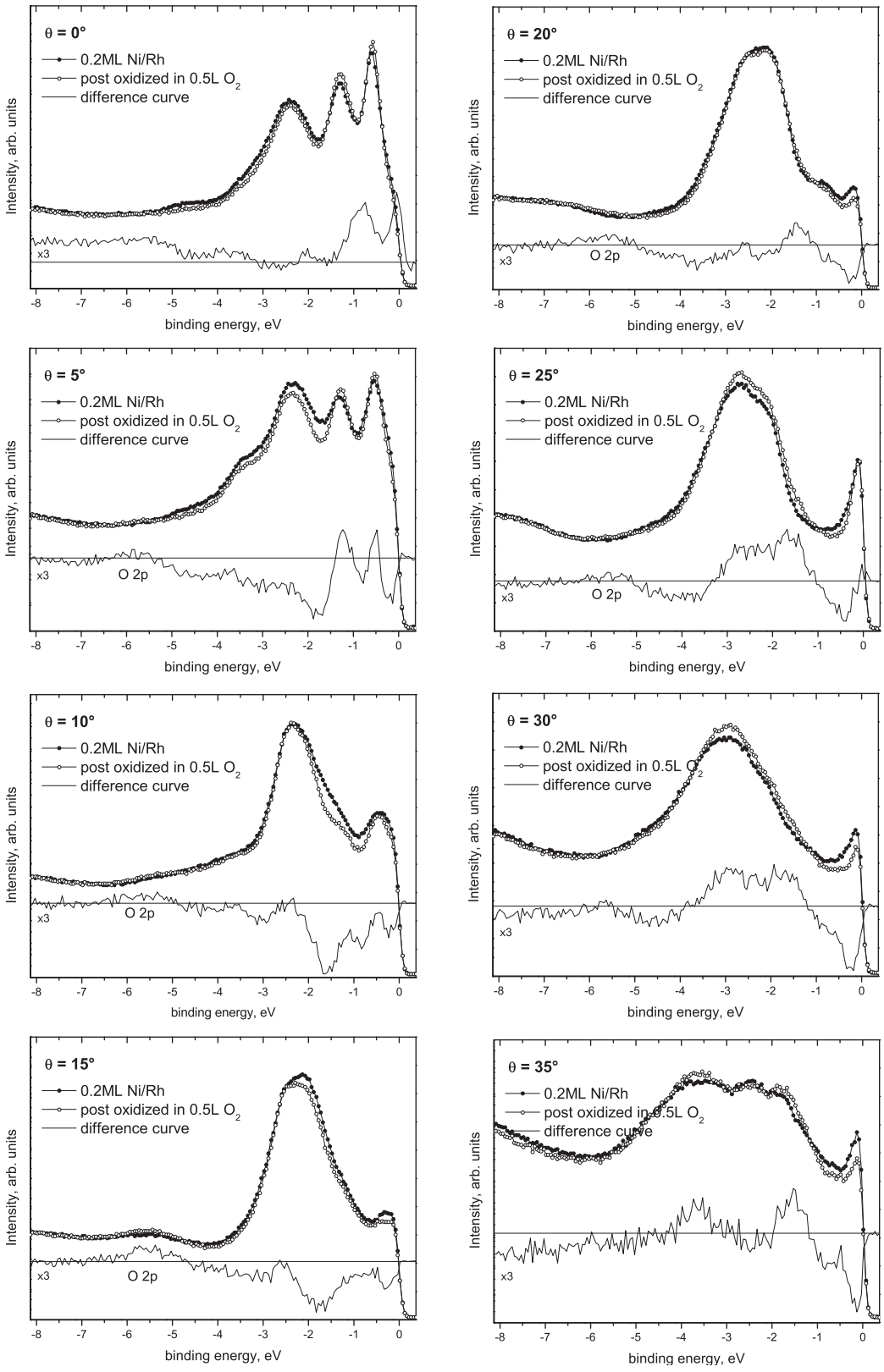

Figure 3.22: UPS spectra of 0.2 ML Ni, oxidized by 0.5 L oxygen, for various emission angles.

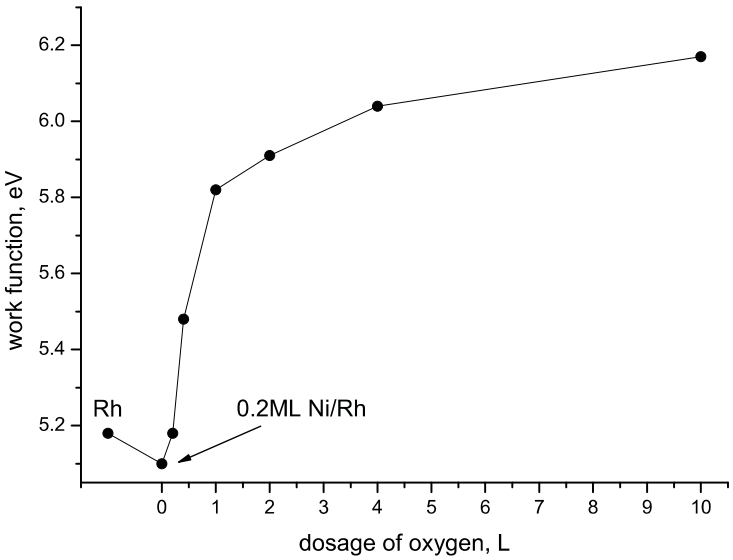

Figure 3.23: Evolution of the work function of 0.2 ML Ni oxidized at 570 K.

the surface is oxidized is very similar to the oxidation of clean Rh(5 5 3): The Rh 4d and Ni 3d states become weaker in intensity when the dosage of oxygen is increased. The peak (1) at 0.5 eV (indicated in the figure) shifts to higher binding energies (with respect to the spectra of the Ni-decorated surface) as a function of the oxygen dosage. The bands (2), (3), and (4) remain at their energy. The reduction of the intensity is not equal in the region of 0–4 eV binding energy: When the dosage increases the peaks (1) and (4) decrease more rapidly than (2) does.
When the valence band of oxidized 0.2 ML Ni/Rh(5 5 3) is compared to oxidized Rh(5 5 3) (the dosage for both surfaces has been 10 L, which means that the terraces of the Ni-decorated surface are covered with oxygen as well) one sees the changes in the region of the Ni bands, as it is illustrated in the difference curves of Fig. 3.25.

3.5.2 Oxidation of Thicker Nickel Films

In the chapter 3.4.3 several coverages of Ni on Rh(5 5 3) have been investigated by LEED and UPS. Consequently, this surfaces have been oxidized as well by 6–10 L of oxygen (5×10^{-8}–10^{-7} mbar oxygen pressure at elevated substrate temperature) in order to get a fully oxidized Ni surface (the bulk of the thicker Ni-films cannot be oxidized since reactive evaporation is nec-

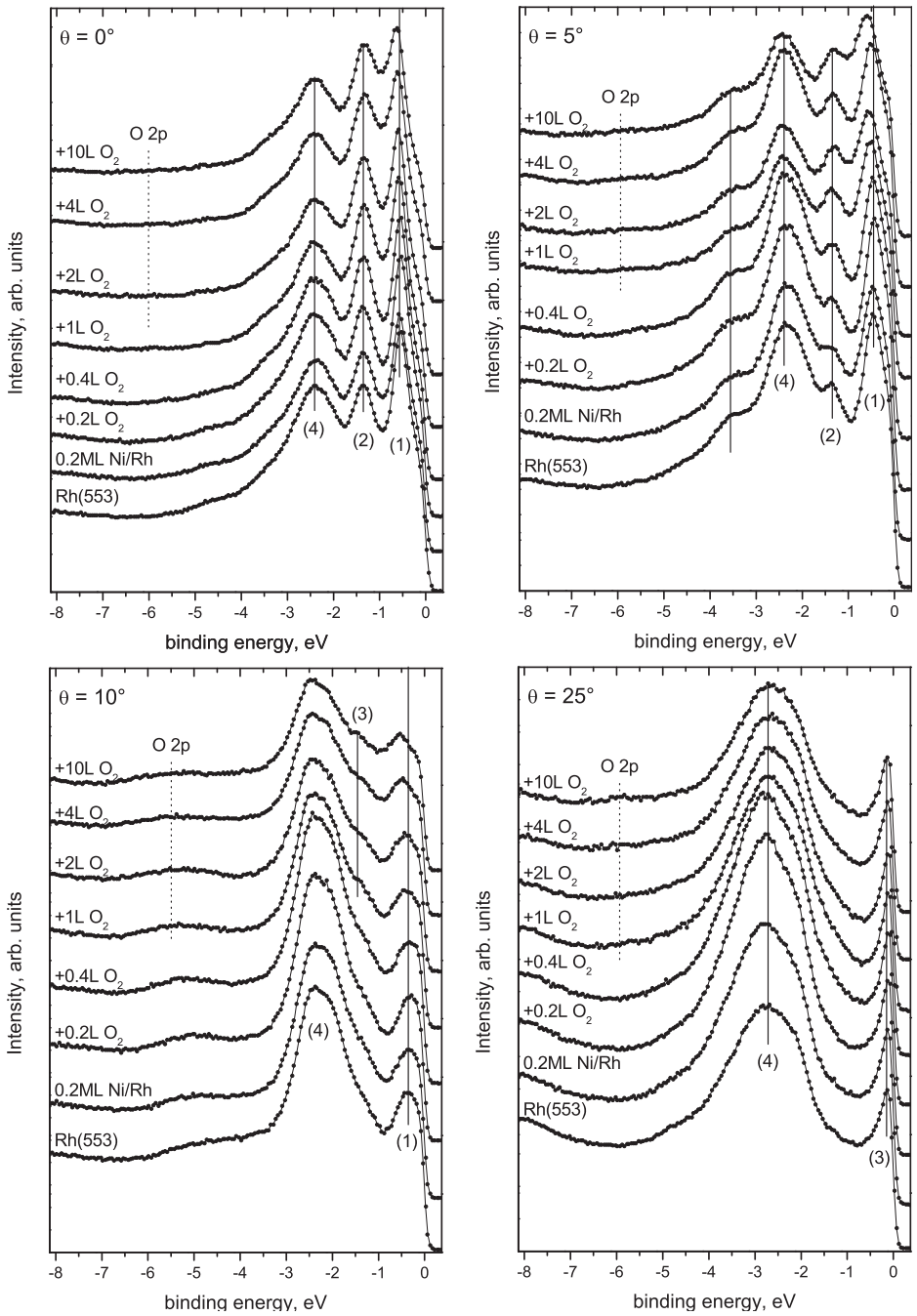

Figure 3.24: UPS spectra of 0.2 ML Ni on Rh(5 5 3), oxidized by 0.2–10 L of oxygen for representative emission angles θ. The bottom curves are clean Rh(5 5 3) for each θ, the next one 0.2 ML Ni on Rh(5 5 3) and then the oxidation starts (0.2 ML Ni + total dosage of oxygen).

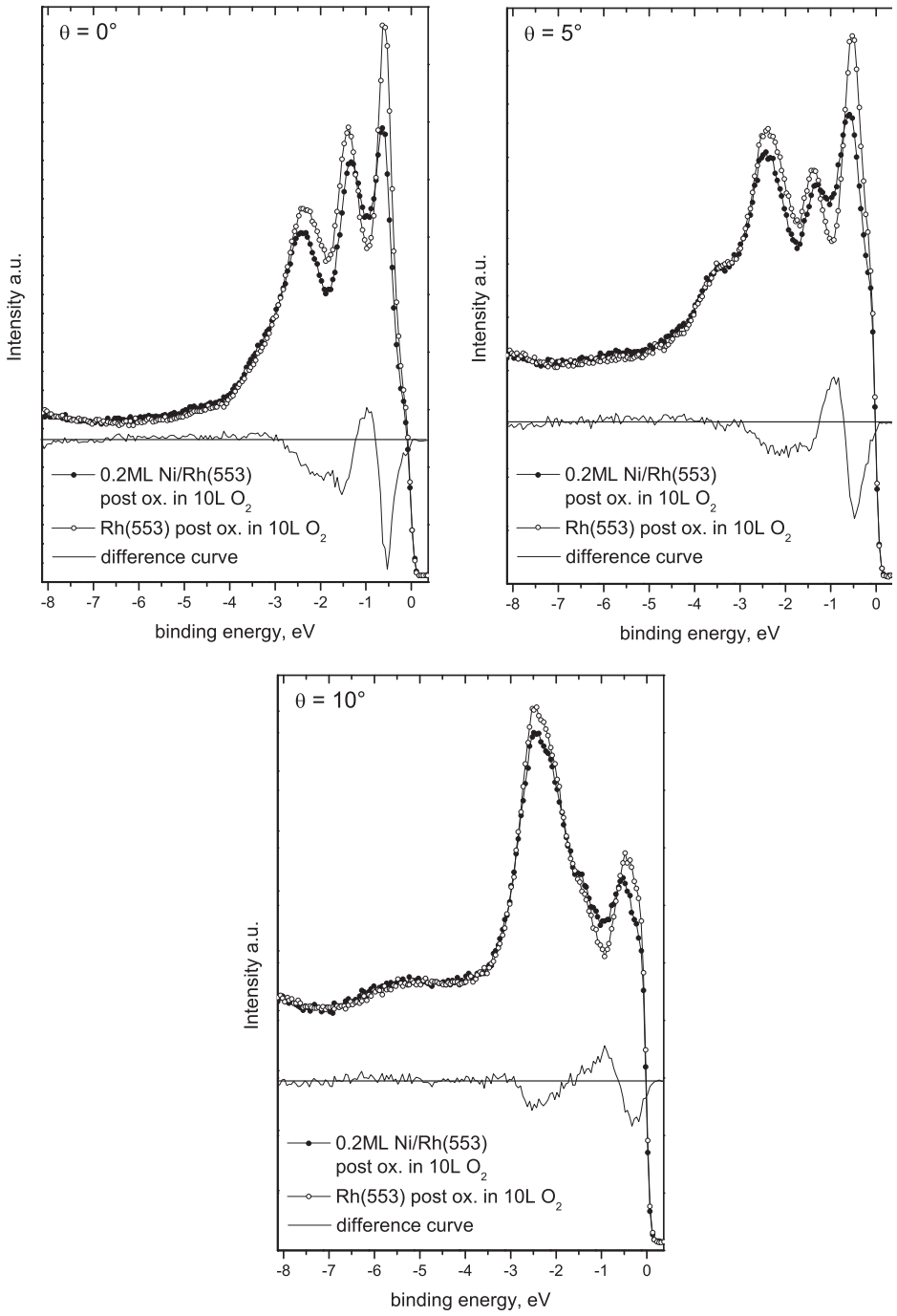

Figure 3.25: UPS spectra of 0.2 ML Ni on Rh(5 5 3) and Rh(5 5 3), both oxidized by 10 L of oxygen. The thin solid curves are the difference curves of oxidized Ni/Rh. minus post-oxidized Rh.

essary). In the following the coverages of 0.4, 0.6, 0.8, 1, 2, 5, and 10 ML of Ni have been studied.

The sub-monolayer decorations behaved all very similar (and produced the same LEED pattern after oxidation in 6–10 L) and the valence band spectra (which are not shown here) show only gradual changes from the spectra of oxidized 0.2 ML Ni to 1 ML Ni. The LEED patterns for the different coverages of Ni with oxidized surfaces are depicted in Fig. 3.26: 0.4–0.8 ML do not differ in the diffraction pattern after the oxidation: The panels (a) and (b) in the figure show the characteristic (2×1) structure (which corresponds to the domain indicated with squares in Fig. 1.7 and Fig. 1.8), which corresponds to oxygen on free Rh-terraces where one domain is prefered by the step direction.
At a coverage of 1 ML of Ni the surface forms a new structure, see panels (c) in Fig. 3.26. The spot-splitting (left LEED pattern) is now a half of the Rh(5 5 3) splitting, which means a periodicity of twice the terrace width.
Increasing the coverage to 2 ML (picture (d)) and oxidized, the diffraction pattern shows a well ordered (2×2) as well as the periodicity of the steps.
When thicker Ni-layers on Rh(5 5 3), such as 5 and 10 ML, are post-oxidized, the surface loses most of its symmetry. The patterns (highly amplified in contrast) show a weak hexagonal symmetry, for 5 ML (Fig. 3.26 (e)) blurred streaks are visible, which possibly indicate a badly ordered (2×2) structure and for some electron energies the splitting of the spots is visible (probably not due to the oxidized surface itself but the Ni-layer and Rh(5 5 3) substrate underneath). The patterns of 10 ML (panels (f) in the figure) do not show the (2×2) symmetry, but a structure, which looks like a (2×1) superlattice with step periodicity (left image) and a moiré-like pattern (right image).

A collection of UPS measurements is plotted in Fig. 3.27: After the oxidation the spectra decrease in intensity with respect to the spectra of the non-oxidized surfaces. The shape of the Ni/Rh(5 5 3) valence band changes minimal, especially for the 1 and 2 ML coverage. For the thicker films the whole intensity of the Rh and Ni bands decreases almost constantly. The peaks of the spectra do not shift in binding energy once the surface is covered with Ni (see the mark at the feature (a) in the figure). The broad O 2p band at 5–5.5 eV is formed.

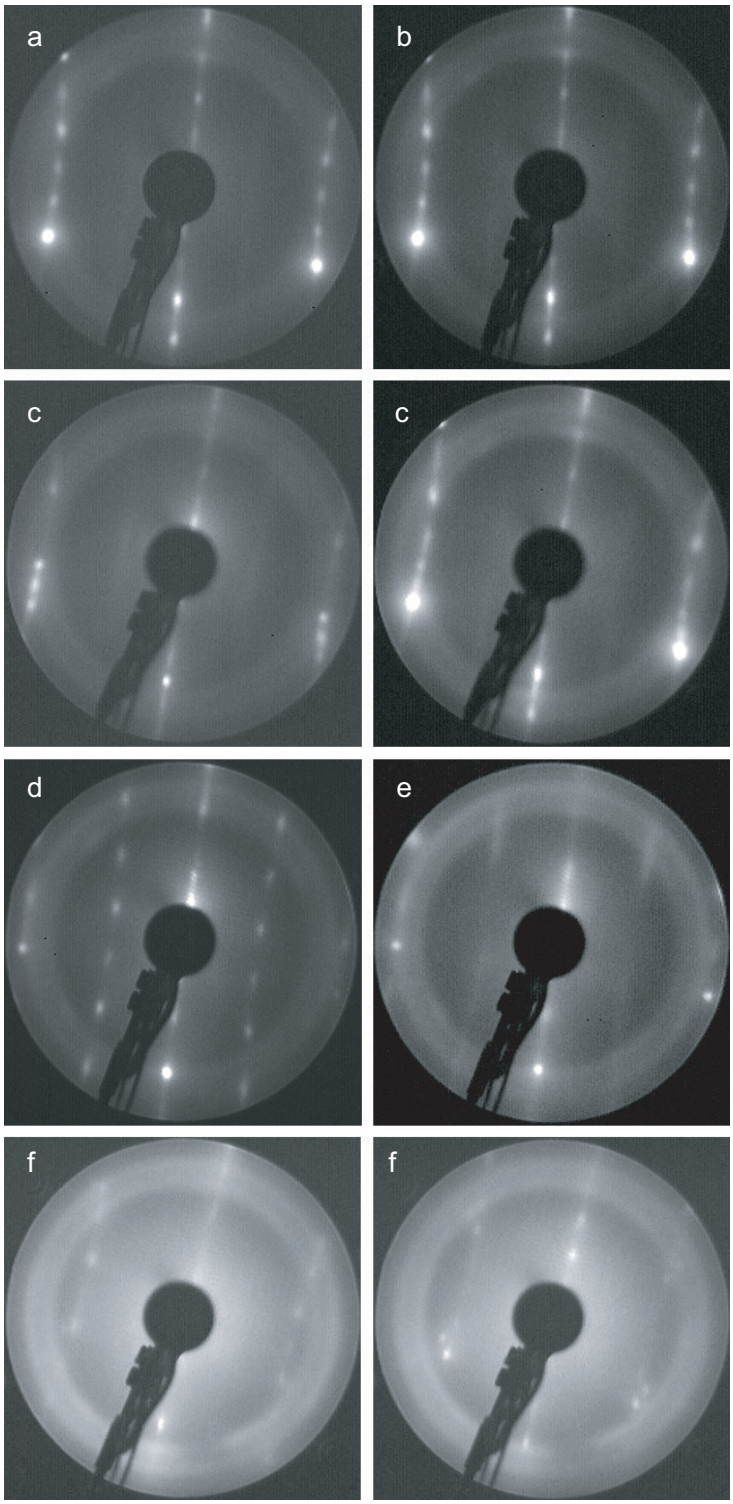

Figure 3.26: LEED pattern of various thick Ni layer on Rh(5 5 3), oxidized by 6–10 L oxygen: (a) 0.6 ML (102 eV), (b) 0.8 ML (102 eV), (c) 1 ML (88 eV and 101 eV), (d) 2 ML (72 eV), (e) 5 ML (75 eV), and (f) 10 ML (147 eV and 178 eV)

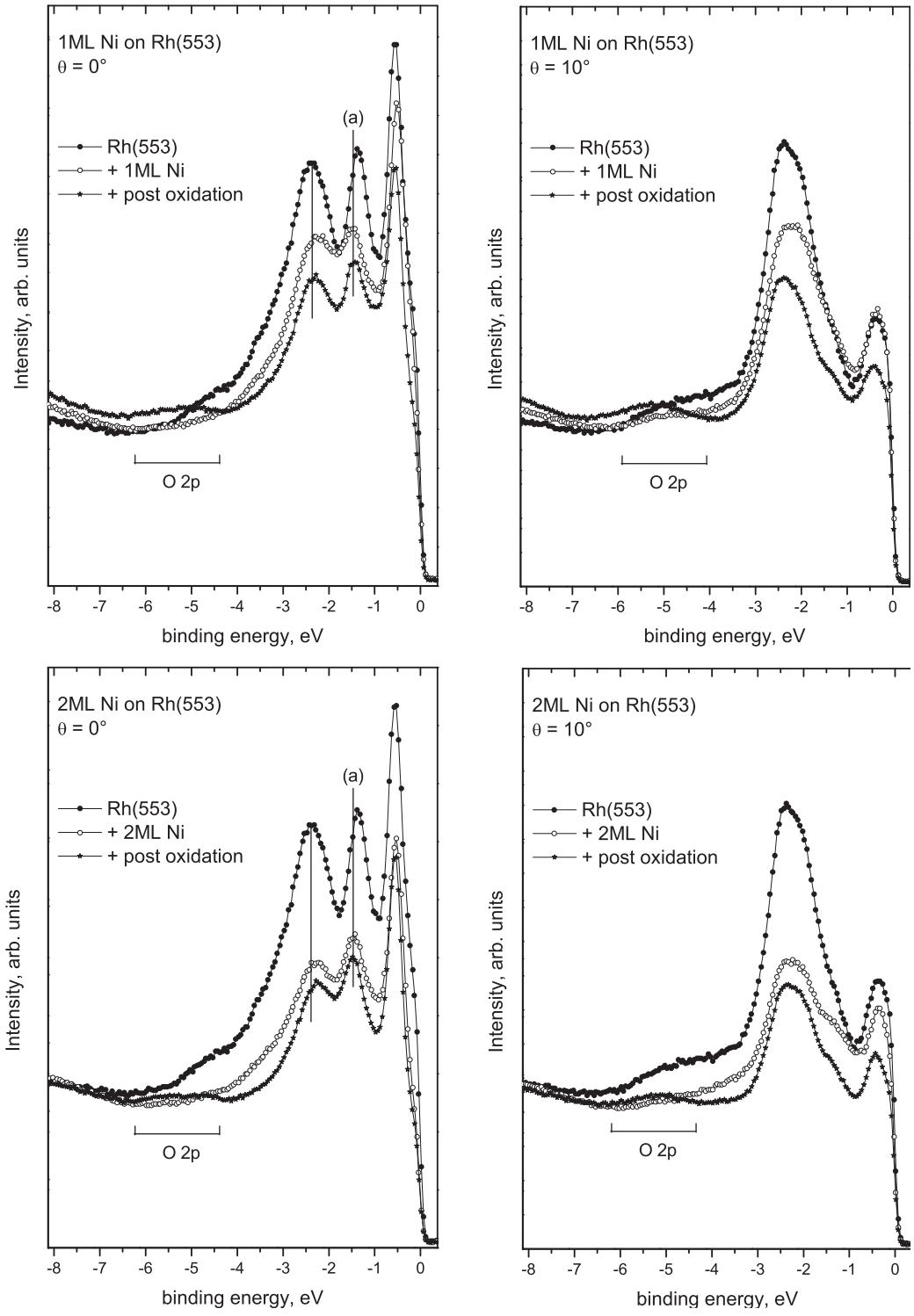

Figure 3.27: Valence band spectra of oxidized 1, 2, 5, and 10 ML Ni on Rh(5 5 3) for two emission angles (normal emission and 10 ° side by side in the figure). (For the second part of the figure see next page.)

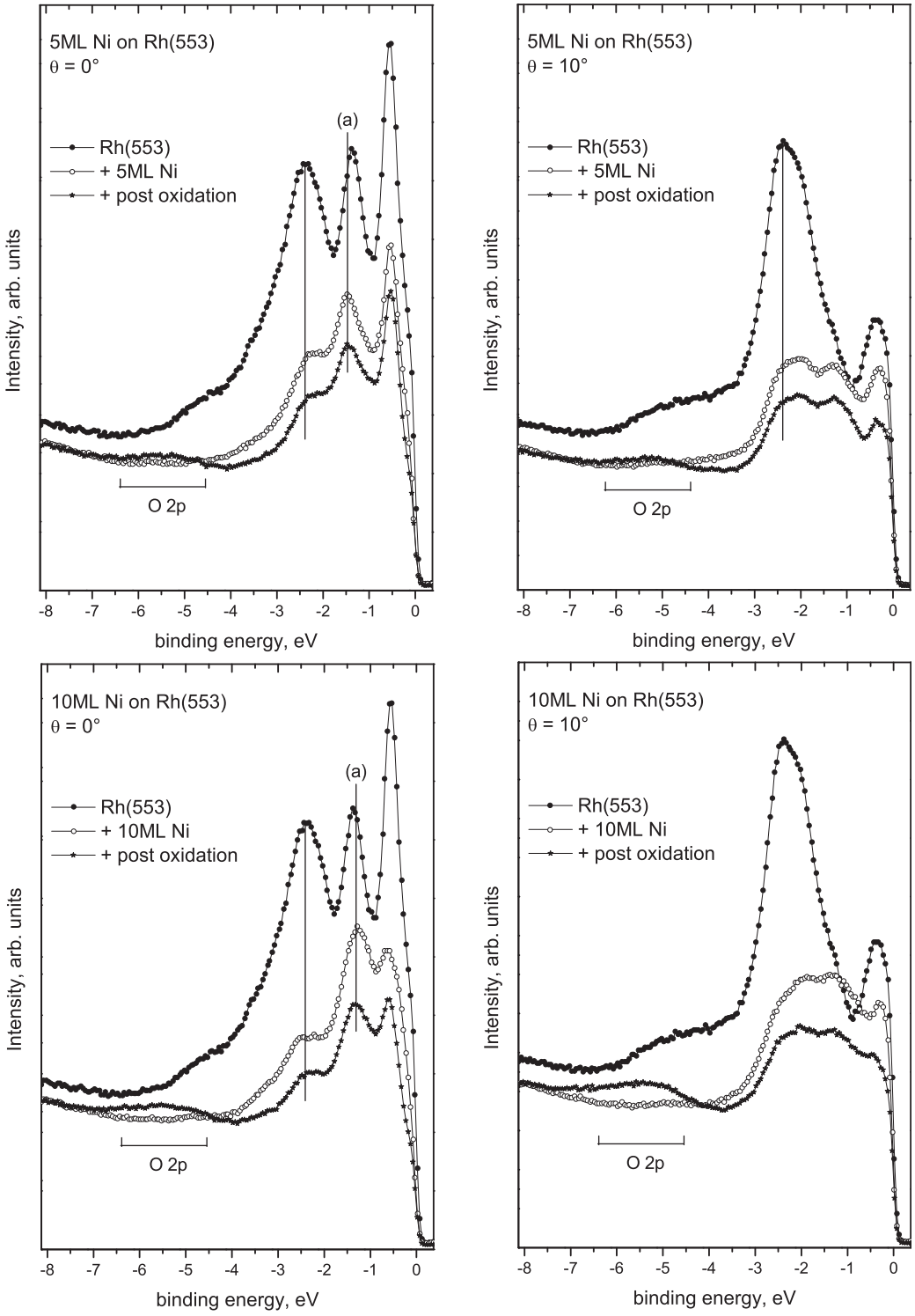
5ML Ni on Rh(553)
θ = 0°
Rh(553)
+ 5ML Ni
+ post oxidation
(a)
O 2p
Intensity, arb. units
binding energy, eV
5ML Ni on Rh(553)
θ = 10°
Rh(553)
+ 5ML Ni
+ post oxidation
O 2p
Intensity, arb. units
binding energy, eV
10ML Ni on Rh(553)
θ = 0°
Rh(553)
+ 10ML Ni
+ post oxidation
(a)
O 2p
Intensity, arb. units
binding energy, eV
10ML Ni on Rh(553)
θ = 10°
Rh(553)
+ 10ML Ni
+ post oxidation
O 2p
Intensity, arb. units
binding energy, eV

Chapter 4

Conclusions

In chapter 3.2.1 the band structure of clean Rhodium(5 5 3) has been measured in the azimuth parallel to the step array and has been compared with DFT calculations, which have been performed by A. Stroppa of the group of F. Mittendorfer of the University of Vienna. It could be shown that a calculation of a 13 layer slab explains most of the features, which are seen in the measured band map. Due to effects of the photoemission cross-section and a strong background of the bulk states some of the calculated terrace and step states are very weakly visible in the room temperature measurements. In addition to the states of the valence band of Rh(5 5 3), a secondary electron resonance could be identified, as in previous investigations on the Rh(1 1 1) surface by [23].
The following chapter 3.2.2 presents the band structure of the clean stepped Rh(5 5 3) surface measured perpendicular to the steps. As expected there is no symmetry around gamma due to the non existing mirror plane symmetry. The band structure contains a contribution of the (1 1 1) terraces (shifted in k-space) which shows mirror symmetry around the normal emission of the terrace ($\approx 12\,^\circ$). The normal emission spectrum of the terraces agrees very well with the normal emission spectrum of a Rh(1 1 1) surface (taken from [23]).

After that the surface has been decorated with Ni atoms, see chapter 3.4. Previous investigations by J. Schoiswohl yielded a routine to decorate only the step edges with 1D Ni-chains. This has been done with 0.2 ML (and 0.4 ML Ni) and the valence band along the Ni wires has been studied angle-resolved. Since the changes in intensity in the measured spectra are small after the decoration of the steps, difference curves have been calculated. They show two little dispersing bands between the Fermi edge and -2 eV binding energy, which are related to the Ni-decoration. Since Ni grows pseudomor-

phously on Rh(5 5 3) it has to expand by 9 % to adopt the Rh lattice constant. This causes little interaction between the Ni atoms along the step edges, which explains the small dispersion of <1 eV of the bands. DFT calculations for 0.2 ML Ni on Rh(5 5 3) agree qualitatively well with the measurement.
In addition to the step decoration in the sub-monolayer range, the growth of Ni thin films (≤10 ML) on Rh(5 5 3) has been studied by LEED and UPS. For coverages ≤2 ML, the diffraction patterns indicate a strong dependence on the substrate symmetry. Thicker layers (up to 10 ML of Ni) show reconstructions. Examining the growth with UPS a gradual transition of the electronic structure from Rh(5 5 3) to a (111)-like Ni surface is obtained: Difference curves of the valence band spectra result in two bands, which can be related to the Ni coverage. The secondary electron resonance, which has been found in the band structure of Rh(5 5 3) measured parallel to the steps, vanished after covering the surface with 2 ML of Ni.

When Ni on Rh(5 5 3) is oxidized it is known from XPS measurements and DFT calculations of the adsorption energies of different sites that the Ni atoms are oxidized first. Therefore it is possible to build Ni-O decorated steps without covering too much of the terraces with oxygen (<0.5 L oxygen). In chapter 3.5.1 the step decoration of 0.2 ML Ni has been oxidized by 0.2 and 0.5 L and the valence band has been studied angle-resolved. The oxidation, which leads to the hybridization of Ni 3d (and Rh 4d) orbitals with the O 2p orbitals, causes small changes and shifts in the region of the Ni bands. After that the same surface has been oxidized by up to 10 L, which covers not only the Ni-chains with oxygen but the Rh-terraces as well. 10 L of oxygen is approximately sufficient to saturate the surface with oxygen, as the valence band spectra and work function indicate.
Chapter 3.5.2 gives an overview on the growth of thicker Ni layer on Rh(5 5 3), which also have been oxidized. The oxygen dosage has been chosen to be 6 L for the sub-monolayer range of Ni, and 10 L for thick films. Although the diffraction patterns show different structures for almost every coverage, the valence band spectra decrease smoothly in intensity and keep the shape of the spectra of the non oxidized Ni-covered surface. The LEED patterns indicate a loss of order on the surface when the coverage of Ni is increased and the disappearance of the spot splitting gives evidence that the influence of the substrate step array has been lost at the surface.

Part III

Appendix

Bibliography

[1] G.E. Moore. Cramming more components onto integrated circuits. *Electronics*, 38, 1965.

[2] J.E. Ortega and F.J. Himpsel. *Lecture Notes in Physics*, chapter Atomic Chains at Surfaces, pages 147–183. Springer Berlin / Heidelberg, 2007.

[3] J.E. Ortega, A. Mugarza, V. Repain, S. Rousset, V. Pérez-Dieste, and A. Mascaraque. One-dimensional versus two-dimensional surface states on stepped Au(1 1 1). *Phys. Rev. B*, 65:165413, 2002.

[4] A. Mugarza and J.E. Ortega. Electronic states at vicinal surfaces. *J. Phys.: Condens. Matter*, 15:3281–3310, 2003.

[5] J.E. Ortega, M. Ruiz-Osés, J. Cordón, A. Mugarza, J. Kuntze, and F. Schiller. One-dimensional versus two-dimensional electronic states in vicinal surfaces. *New Journal of Physics*, 7:101, 2005.

[6] S. Shiraki, H. Fujisawa, M. Nantoh, , and M. Kawai1. Confining Barriers for Surface State Electrons Tailored by Monatomic Fe Rows on Vicinal Au(1 1 1) Surfaces. *Phys. Rev. Letters*, 92:096102, 2004.

[7] H. Fujisawa, S. Shiraki, M. Furukawa, S. Ito, T. Nakamura, T. Muro, M. Nantoh, and M. Kawai. Electronic structure and magnetism of one-dimensional Fe monatomic wires on Au(7 8 8) investigated with ARPES and XMCD. *Phys. Rev. B*, 75:245423, 2007.

[8] J. Gustafson, A. Resta, A. Mikkelsen, R. Westerström, J.N. Andersen, E. Lundgren, J. Weissenrieder, M. Schmid, P. Varga, N. Kasper, X. Torrelles, S. Ferrer, F. Mittendorfer, and G. Kresse. Oxygen-induced step bunching and faceting of Rh(5 5 3): Experiment and ab *initio* calculations. *Phys. Rev. B*, 74:035401, 2006.

[9] J. Schoiswohl, F. Mittendorfer, S. Surnev, M.G. Ramsey, J.N. Andersen, and F.P. Netzer. Chemical Reactivity of Ni-Rh Nanowires. *Physical Review Letters*, 97:126102, 2006.

[10] J. Schoiswohl, F. Mittendorfer, S. Surnev, M.G. Ramsey, J.N. Andersen, and F.P. Netzer. The self-assembly of metallic nanowires. *Surface Science Letters*, 600:L274–L280, 2006.

[11] J. Schoiswohl. *Vanadium- and nickel-oxides nanostructures on physically patterned rhodium and palladium surfaces*. PhD thesis, Karl-Franzens-Universität Graz, Austria, 2006.

[12] M.A. Van Hove, W.H. Weinberg, and C.M. Chan. *Low Energy Electron Diffraction*. Springer Verlag Berlin-Heidelberg, 1986.

[13] S. Hüfner. *Photoelectron Spectroscopy, Principles and Application*. Springer-Verlag Berlin Heidelberg, 1995.

[14] M. Giesen and T.L. Einstein. Analysis of Terrace Width Distributions on Vicinal Copper Surfaces Using the Wigner Surmise: Comparison with Gaussian Approximation. *Surface Sci.*, 499:191–206, 2000.

[15] J.M. Howe. *Interfaces in Materials*. John Wiley & Sons, Inc., 1997.

[16] Hans Lüth. *Surfaces and Interfaces of Solids*. Springer-Verlag, 1993.

[17] Andrew Zangwill. *Physics at Surfaces*. Cambridge University Press, 1988.

[18] M. Horn von Hoegen. Growth of semiconductor layers studied by spot profile analysing low energy electron diffraction—part i. *Z. Kristallogr.*, 214:591–626, 1999.

[19] H. Pietsch F.-J. Meyer zu Heringdorf and M. Horn von Hoegen. Reciprocal Space Mapping by spot profile analyzing low energy electron diffraction. *Rev. Sci. Instrum.*, 76:085102, 2005.

[20] M. Henzler and W. Göpel. *Oberflächenphysik des Festkörpers*. B.G. Teubner Stuttgart, 1991.

[21] G. Ertel and J. Küppers. *Low Energy Electrons and Surface Chemistry*. VCH Verlagsgesellschaft, 1985.

[22] A. Beutler, E. Lundgren, R. Nyholm, J.N. Andersen, B.J. Setlik, and D. Heskett. Coverage- and temperature-dependent site occupancy of carbon monoxide on Rh(111) studied by high-resolution core-level photoemission. *Surface Science*, 396:117–136, 1998.

[23] A. Goldmann, G. Rosina, E. Bertel, and F.P. Netzer. The electronic structure of Rhodium: Angle-resolved studies of photoelectron and secondary electron emission. *Zeitschrift für Physik B Condensed Matter*, 73:479–487, 1989.

[24] G.R. Castro, H. Busse, U. Schneider, T. Janssens, and K. Wandelt. Geometric and Electronic Structure of Potassium on Rh(1 1 1). *Phys. Scr.*, 499:208–212, 1992.

[25] F.J. Himpsel, J.A. Knapp, and D.E. Eastman. Angle-resolved photoemission study of the electronic structure of chemisorbed hydrogen on Ni(1 1 1). *Phys. Rev. B*, 19:2872–2875, 1979.

[26] N. Fischer, S. Schuppler, Th. Fauster, and W. Steinmann. Intrinsic linewidths of image-potential states on Ni(1 1 1). *Phys. Rev. B*, 42:9717–9719, 1990.

Acknowledgment

I would like to thank Prof. F. Netzer for the opportunity of doing my diploma in his group.
My thanks also goes to S. Berkebile for his introduction to the ADES system, the whole group for their help and assistance, and F. Stroppa and F. Mittendorfer from the University of Vienna for the DFT-calculations.

This work has been supported by the Austrian Research Funds through the National Research Network "Nanoscience on Surfaces".